REPORT DOCUMENTATION PAGE

Form Approved
OMB No. 0704-0188

1. AGENCY USE ONLY (Leave blank)	2. REPORT DATE	3. REPORT TYPE AND DATES COVERED
	14 Sep 95	Final Sep 92 - Aug 95

4. TITLE AND SUBTITLE
Student Training Program in Advanced Diagnostics for High-Speed Fluid Mechanics.

5. FUNDING NUMBERS
F49620-92-J-0335

6. AUTHOR(S)
Richard Miles

7. PERFORMING ORGANIZATION NAME(S) AND ADDRESS(ES)
Princeton University

8. PERFORMING ORGANIZATION REPORT NUMBER
AFOSR-TR-96-0029

9. SPONSORING/MONITORING AGENCY NAME(S) AND ADDRESS(ES)
AIR FORCE OFFICE OF SCIENTIFIC RESEARCH
DIRECTORATE OF AEROSPACE SCIENCES
BOLLING AFB, DC 20332-6448
NA

10. SPONSORING/MONITORING AGENCY REPORT NUMBER
F49620-92-J-0335

11. SUPPLEMENTARY NOTES

12a. DISTRIBUTION/AVAILABILITY STATEMENT
APPROVED FOR PUBLIC RELEASE
DISTRIBUTION IS UNLIMITED

12b. DISTRIBUTION CODE

13. ABSTRACT *(Maximum 200 words)*

As described in previous reports, this AASERT funding has provided support for graduate student training in high-speed optical flow diagnostics. Funds were provided for the purchase of a 20 MHz rate framing camera (Hadland Imacon 792), which was used to capture a pair of rapidly sequenced Rayleigh scattering images, using a double-pulsed Nd:YAG laser system purchased form parent grant AFOSR support. During the current reporting period, work has progressed on a synergistic program to develop a "burst mode" laser system, which will, ultimately, provide the capability to obtain approximately 30 rapidly sequenced images. This work is closely coupled with the parent grant (#F496200-92-J-0217) and a collaborative AFOSR program with Profs. Alexander Smits and Garry Brown (F49620-93-1-0064).

14. SUBJECT TERMS	15. NUMBER OF PAGES
GRADUATE STUDENT TRAINING	33
	16. PRICE CODE

17. SECURITY CLASSIFICATION OF REPORT	18. SECURITY CLASSIFICATION OF THIS PAGE	19. SECURITY CLASSIFICATION OF ABSTRACT	20. LIMITATION OF ABSTRACT
UNCLASSIFIED	UNCLASSIFIED	UNCLASSIFIED	UL

PRINCETON UNIVERSITY
Department of Mechanical & Aerospace Engineering
Princeton, New Jersey 08544'

"STUDENT TRAINING PROGRAM IN ADVANCED DIAGNOSTICS FOR HIGH-SPEED FLUID MECHANICS"

FINAL YEARLY PROGRESS REPORT TO:

Dr. Leonidas Sakell
Program Director
AIR FORCE OFFICE OF SCIENTIFIC RESEARCH/NA
A-225, Building 410
Bolling Air Force Base
Washington, DC 20332-6448

AASERT GRANT #F49640-92-J-0335

Reporting Period: September 1994 to August 1995

Richard B. Miles, Professor
Princeton University
Principal Investigator

September 14, 1995

(150-6644)

STUDENT TRAINING PROGRAM IN ADVANCED DIAGNOSTICS FOR HIGH-SPEED FLUID MECHANICS

AASERT Grant #F49640-92-J-0335

Final Year Progress Report

As described in previous reports, this AASERT funding has provided support for graduate student training in high-speed optical flow diagnostics. Funds were provided for the purchase of a 20 MHz rate framing camera (Hadland Imacon 792), which was used to capture a pair of rapidly sequenced Rayleigh scattering images, using a double-pulsed Nd:YAG laser system purchased form parent grant AFOSR support. During the current reporting period, work has progressed on a synergistic program to develop a "burst mode" laser system, which will, ultimately, provide the capability to obtain approximately 30 rapidly sequenced images. This work is closely coupled with the parent grant (#F496200-92-J-0217) and a collaborative AFOSR program with Profs. Alexander Smits and Garry Brown (F49620-93-1-0064).

During the current reporting period, AASERT funds have been used to support a new Air Force program to explore the potential of a radiatively-driven hypersonic wind tunnel facility. The AASERT graduate student (Mr. George Williams) has been responsible for one-dimensional modeling of non-isentropic expansions under highly non-ideal gas conditions. His work is documented in detail in the attached two reprints (Appendix A), and we will, therefore, summarize the principal results below.

A. Results: Radiative Driven Wind Tunnel

A convenient way of viewing the operation of such a facility is with the help of a Mollier diagram (Fig. 1). In this diagram, the enthalpy is plotted versus the entropy. For a conventional wind tunnel facility, the expansion is assumed to be isentropic, so the static temperature and pressure and the Mach number in the test chamber mandate a unique temperature and pressure for the gas in the plenum. For example, for a Mach 16 flow with a static temperature of 200 K and a static pressure of 10^{-3} atm (150,000'--point C on the diagram), the plenum must be held at a temperature of 6300 K, and at a pressure of 4000 atm (Point A). Clearly, at this temperature, air is highly dissociated and severe problems with containment and throat erosion occur. In contrast, the radiatively-driven wind tunnel begins with a plenum pressure on the order of 30,000 atm, but a plenum temperature on the order of 1000 K. The point on the Mollier diagram (Point B) associated with this initial condition corresponds to significantly lower entropy and lower

enthalpy than that of the isentropic wind tunnel. That remaining enthalpy and entropy is then added downstream of the throat using the radiative source.

George Williams' work has focused on development and application of a one-dimensional, real gas equation-of-state, flow model which incorporates energy addition and uncoupled NO_x kinetics. He has explored a variety of potential energy sources, including the HF laser at 2.7 microns, which couples to air through the order 100's ppm of naturally occurring CO_2; 60 GHz microwave radiation, which couples directly to molecular oxygen; and high energy (2-20 MeV) electron beams, which couple by inelastic electron-neutral collisions. In the case of laser energy, the beams are assumed to propagate in the upstream direction from an initial location in the vicinity of a test section. The model incorporates refraction effects, due to the large index-of-refraction gradients which would exist in a thermal boundary layer, and which cause the beams to be steered toward the flow centerline.

A detailed description of the individual elements of the 1D code, as well as a series of illustrative results for a full-scale facility using HF laser radiation has been recently published in the AIAA Journal (reprint attached). In addition to fluid phenomena (i.e., that which can be described through continuity equations), the radiatively-driven wind tunnel concept requires detailed knowledge of a variety of molecular phenomena, in particular, optical absorption and energy thermalization. While the phenomenology of these effects is well understood, many details have not been explored in the temperature and pressure regimes relevant to the radiative wind tunnel concept. We have begun an experimental and modeling effort to address the most important issues, preliminary results of which were presented at the 30th AIAA Thermophysics Conference, June 1995 (San Diego, California). (Reprint attached.)

Recently, our Air Force sponsors have expressed interest in smaller scale demonstration experiments which would serve to demonstrate the principle and to validate modeling efforts (both 1D and axisymmetric). These experiments would require sources capable of output power on the order of 1 MWatt for time durations on the order of 0.1-1.0 seconds. Possible sources include a high power DF laser at White Sands, New Mexico, a 2 MeV electron beam facility at Sandia National Laboratories in Albuquerque, New Mexico, and a 1 MWatt, 110 GHz microwave gyration, at either General Atomics (San Diego, CA), or Varian (Palo Alto, California).

Figures 2-5 shows some recent modeling predictions for a 2 MeV electron beam source in which the final total enthalpy corresponds to approximately 200% of the stagnation enthalpy. The stagnation conditions are 1000 atm P, 500 K, which corresponds to an enthalpy of approximately 0.5 MJ/kgm of air.

Figures 2-5 show the 1D code results for nozzle radius, free stream velocity, and free stream static pressure and temperature, respectively. In this case, the code was constrained to solve the continuity equations for a constant Mach number expansion until a static temperature of 400 K was achieved. At this point, the expansion was constrained to isothermal.

It can be seen that a relatively gentle expansion, from diameter 2.4 to 10 mm over a length of 0.10 m, is required to accommodate the increased enthalpy from the electron beam.

Figures 2-5 are meant to serve as illustrative examples only. In particular, we are now in the process of assembling an axisymmetric, two-dimensional code which will be the next generation design tool.

B. Pulse Burst Laser

While there has been enormous progress in recent years in the development and application of diagnostic imaging techniques, the ability to capture time-evolving or volumetric information is severely constrained by limitations of available laser technology. As a general rule, in the gas phase, signal levels for demonstrated imaging diagnostic techniques are sufficiently small that the measurements require high-power, nanosecond duration pulsed sources, such as Q-switched solid-state (principally Nd:YAG) or excimer lasers. The pulse repetition rate of these devices is limited to the range 10-30 pulses/second for solid-sate lasers, and 10-300 pulses/second for excimer lasers. The current state-of-the-art is represented by double-pulsed Nd:YAG lasers, which may be used to produce a pair of excitation sheets, separated in time between 1-80 microseconds, to capture two sequential images. We are actively engaged in a research effort which will lead to the development of a high-power, Nd:YAG-based, "pulse burst" laser system. The current system is capable of creating a "train" of on the order of 30-40 high power pulses, at a burst frequency of up to 1 MHz. The number and interpulse spacing of the individual pulse is flexible, and individual pulse energies on the order of 10's to 100's of mJ's are, ultimately, anticipated.

The pulse burst laser system illustrated in Fig. 6 consists of the following four elements:

1. Monolithic, single-frequency, diode-pumped, cw Nd:YAG laser.
2. Pulse slicer.
3. Two-stage, multi-pass preamplifier.
4. Two-stage power amplifier.

The single-frequency Nd:YAG laser is a Lightwave Electronics model 120-03, with cw power of approximately 20 mWatts. The output of this laser is polarization-coupled into preamplifier #1, which is a four-pass, 10 Hz repetition rate, flashlamp-pumped, 7 mm diameter by 110 mm long Nd:YAG rod. The small signal, single pass gain has been measured to be approximately 10x, so that the output of preamplifier #1 is a single, approximately 100 microsecond duration, 200 Watt peak power pulse, repeated at a repetition rat e of 10 Hz. This 100 microsecond pulse is formed into a "train" using a pulse slicer, custom built by Medox, Inc., Ann Arbor, Michigan. The pulse slicer consists of a pair of fast electro-optic Pockel cells, and is capable of creating an arbitrary number of pulses, with minimum individual pulse duration of 10 nsec, and minimum inter-pulse period of 1 micro-second. The output of the pulse slicer is spatially filtered and double-passed through preamplifier #2. To date, we have obtained 10^6 net power gain out of this system, with pulse trains consisting of 10-20 pulses, and individual pulse durations between 10-20 nsec. This corresponds to individual pulse energies between 200-400 microjoules.

The above described system has existed in our laboratory for approximately six months, and its operation is relatively straight-forward. The number, spacing, and duration of the pulses within the train can be continuously varied by flipping a few thumbwheel switches on the slicer timing electronics. At the two-stage power amplifier has recently become available and we are currently in the process of incorporating it into the system.

An important feature of the laser system is that the very narrow linewidth makes it a viable source for Filtered Rayleigh Scattering (FRS) measurements. In this case, the frequency is tuned so that the second harmonic overlaps an absorption line of iodine molecular vapor. When an iodine cell is placed in front of the camera system, background scattering at the laser frequency is removed from the image. Light scattered from the flowing gas, however, is frequency shifted due to the Doppler effect, passes through the cell, and is imaged by the camera. In this manner, the time evolution of complex flows near walls an in ducts can be imaged, flow velocity and temperature may also be measured if the cw injection laser is augmented so that it can be rapidly tuned, leading to a frequency-chirped pulse burst. An example of a Filtered Rayleigh image of a

complex flow field inside a duct is shown in Fig. 7. In this case, the scattering is from condensate ice crystals in a Mach 3 flow entering an inlet which has a flat top and bottom, and side fins turned 11° to the flow. The image shows individual cross sections normal to the flow taken at 1/10th of an inch intervals, passing through a crossing shock region. In these images, boundary layer structure and shock curvature are clearly evident. A similar image taken with a pulse-burst laser swept with the flow could follow the evolution of an individual boundary layer structure through the crossing shock region.

The results to-date on our pulse-burst system have been accepted for presentation at the 34th AIAA Aerospace Sciences Meeting in Reno, Nevada (January 1996).

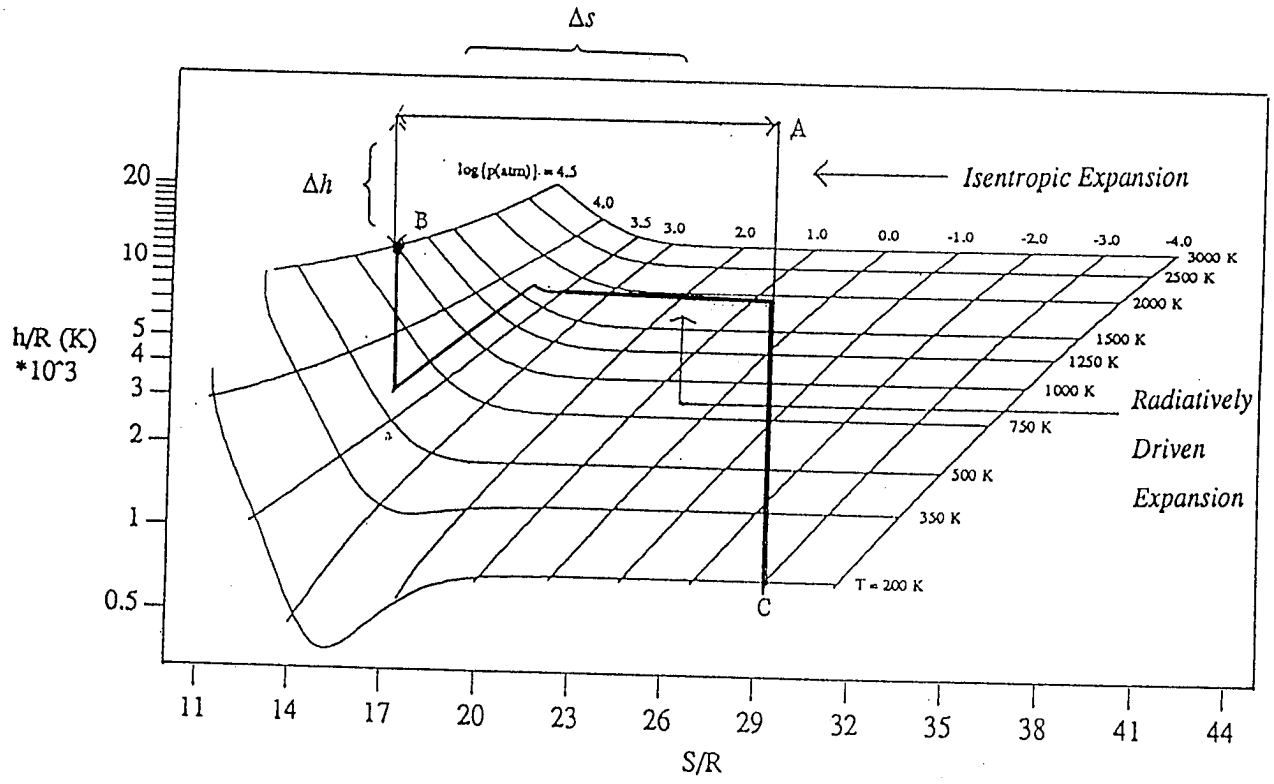

Figure 1. Concept Definition: Thermodynamic Comparison of Wind Tunnel Philosophies.

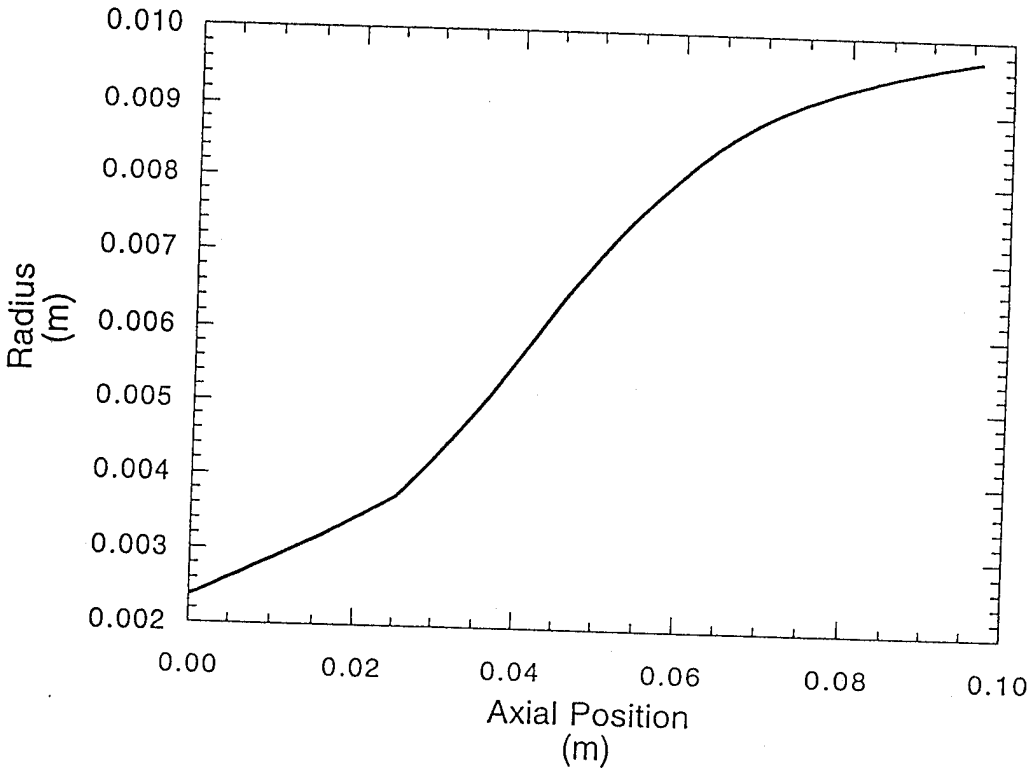

Figure 2. Nozzle radius as a function of downstream position for possible 2 MeV e-beam experiment.

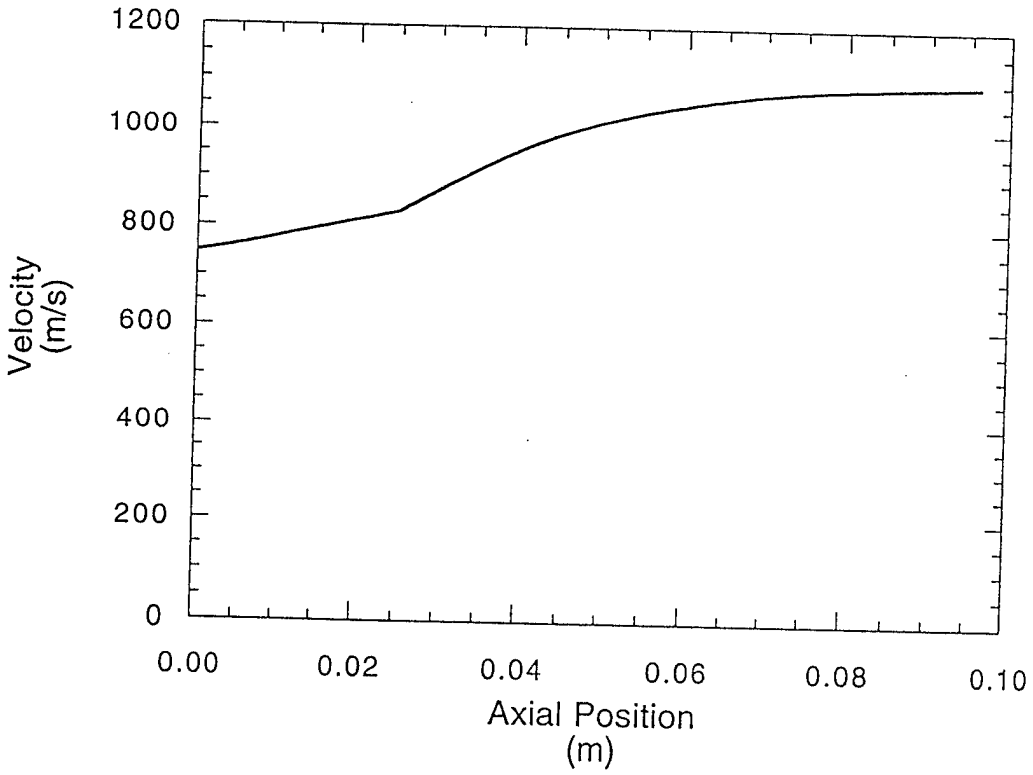

Figure 3. Velocity as a function of downstream position for possible 2 MeV e-beam experiment.

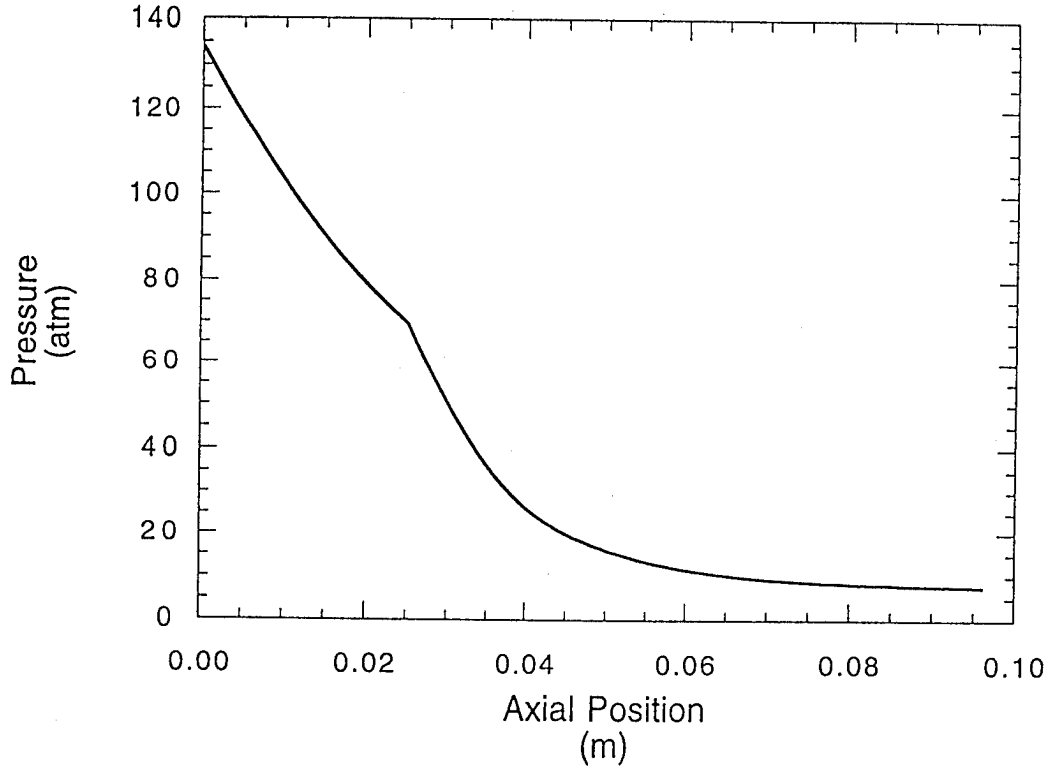

Figure 4. Static pressure as a function of downstream position for possible 2 MeV e-beam experiment.

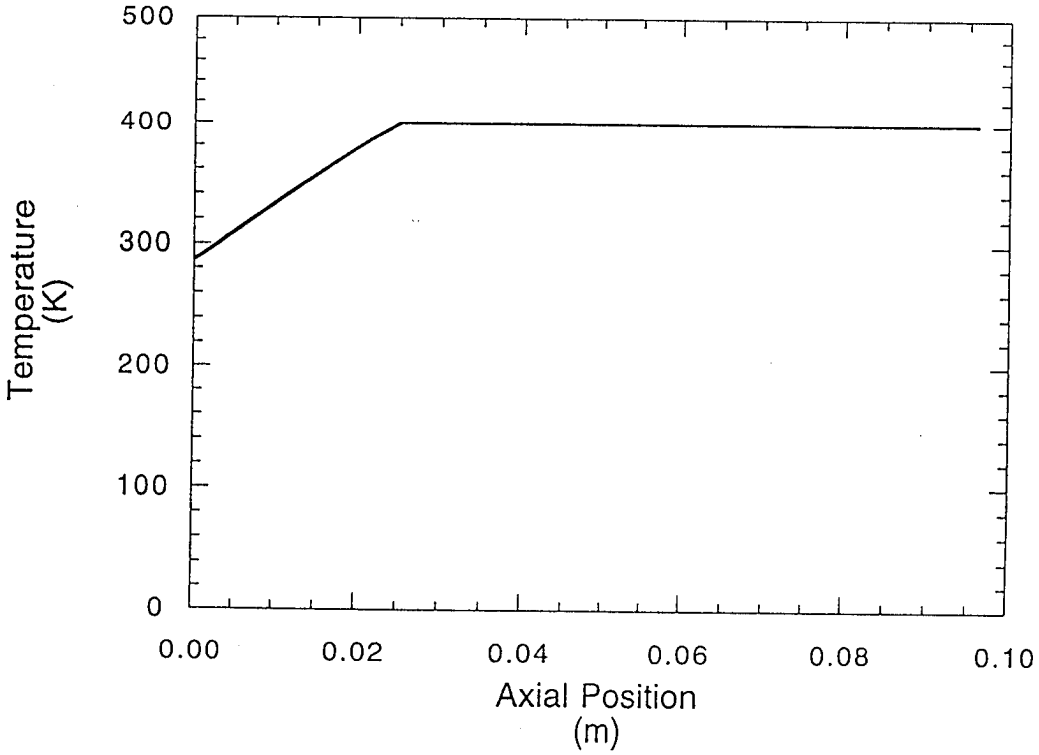

Figure 5. Static temperature as a function of downstream position for possible 2 MeV e-beam experiment.

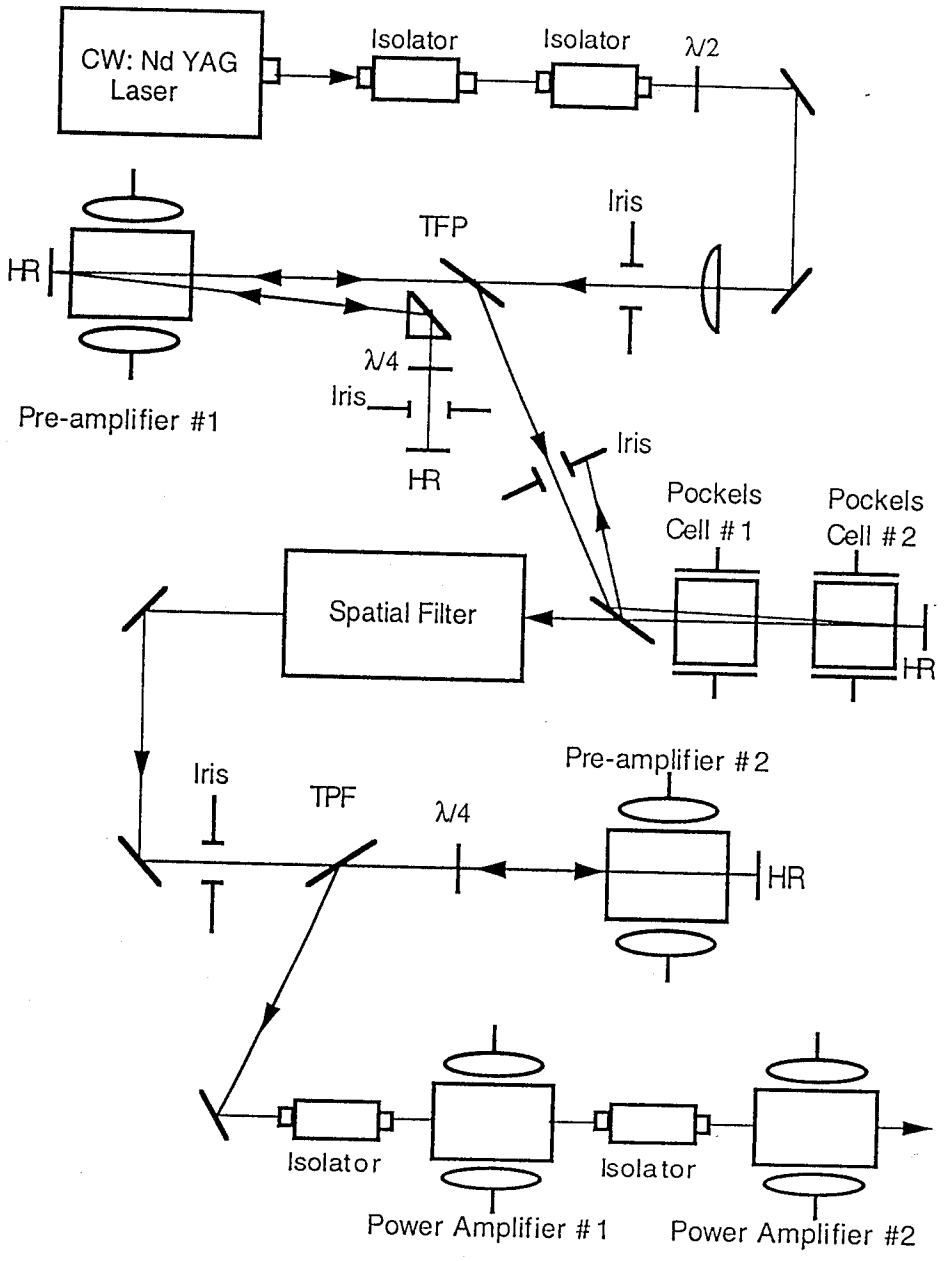

Figure 6. Schematic Diagram of Pulse-Burst Laser System.

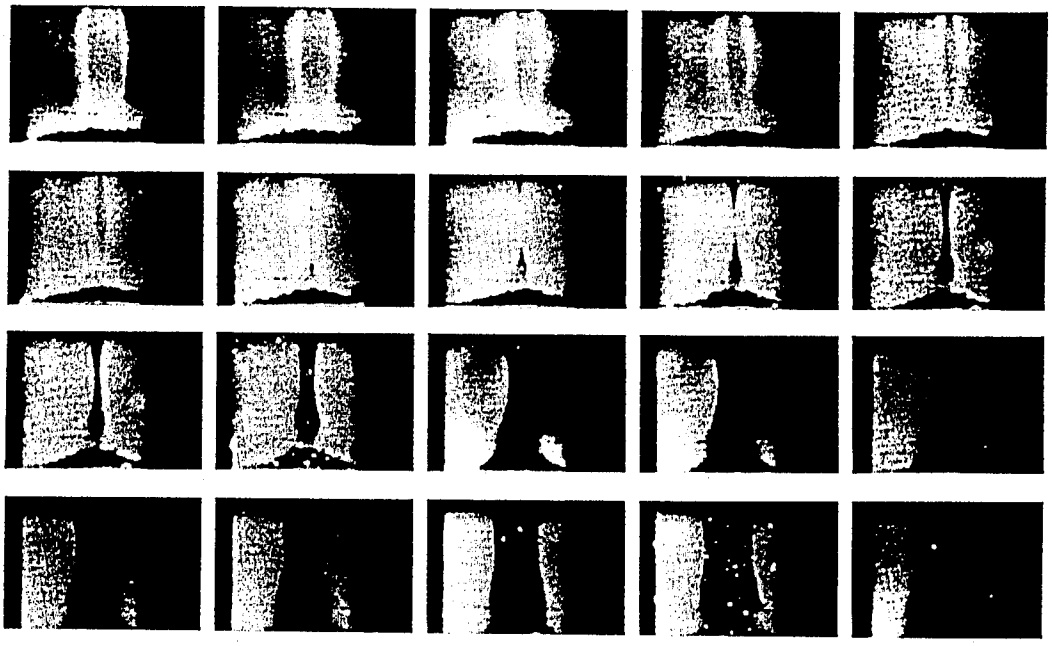

Figure 7. Cross-sectional Filtered Rayleigh images taken at sequential 0.1 inch intervals moving downstream through the shock crossing region of an inlet model.

APPENDIX A -- Reprints

1. R.B. Miles, G.L. Brown, W.R. Lempert, R. Yetter, G.J. Williams, Jr., S.M. Bogdonoff, D. Natelson, and J.R. Guest, "Radiatively Driven Hypersonic Wind Tunnel," AIAA Journal, Vol. 33, No. 8, August 1995, pp. 1463-1470.

2. S. Macheret, G. Williams, G. Comas, C. Meinrenken, W. Lempert, and R. Miles, "Energy Addition and Thermalization Issues in a Radiatively-Driven Hypersonic Wind Tunnel," Paper #AIAA 95-2142, 30th AIAA Thermophysics Conference, June 19-22, 1995, San Diego, CA.

AIAA JOURNAL
Vol. 33, No. 8, August 1995

Radiatively Driven Hypersonic Wind Tunnel

Richard B. Miles,* Garry L. Brown,† Walter R. Lempert,‡ Richard Yetter,§ George J. Williams Jr.,¶ and Seymour M. Bogdonoff‖
Princeton University, Princeton, New Jersey 08544
Douglas Natelson**
Stanford University, Stanford, California 94305
and
Jeffrey R. Guest††
University of Michigan, Ann Arbor, Michigan 48109

This paper outlines a new approach to the design of hypersonic wind tunnels. This new approach is motivated by fundamental limitations of conventional isentropic expansions that arise from the very high temperatures required to achieve the necessary enthalpy for hypersonic flow. These high temperatures lead to excessive throat degradation and contaminated air in the test section. The consequence is that the run times of conventional facilities must be short, and tests are conducted in "air" of unknown composition containing exceedingly high concentrations of radical and superequilibrium species such as NO as well as ablated plenum and throat material. The radiatively driven wind-tunnel approach takes advantage of the real gas properties of air to achieve high enthalpy at low temperature in the plenum, thus minimizing throat degradation and suppressing the formation of unwanted species in the plenum. Additional energy is radiatively added downstream of the throat in the expansion section to achieve the desired test conditions. The temperature of the air is kept low throughout the expansion, so that the formation of superequilibrium species and radicals is kept to a minimum. Radiative sources that couple to air include high-power lasers and microwave devices. A one-dimensional model including optical coupling is developed using, as an example, an HF laser coupled to the naturally occurring CO_2 in air.

Introduction

THE testing and evaluation of hypersonic airplane components and air-breathing propulsion systems are seriously limited by the availability of satisfactory ground test facilities. At Mach numbers higher than approximately Mach 10, tests under true simulated flight conditions, including correct atmospheric temperature and density, cannot be done with current or projected facilities. This limitation occurs because, in the conventional isentropic expansion-type wind-tunnel facility, temperatures in excess of 3000 K are required to achieve static temperatures on the order of 200 K or higher associated with true flight conditions. At these temperatures, the air cannot be contained for long periods of time due to materials limitations, and significant throat erosion occurs during wind-tunnel operation. In addition, radical and superequilibrium species such as NO are formed at high temperature and are frozen into the flowfield in the expansion, contaminating the flow. The solution to these problems has been to operate with very short run times to preserve the throat and to accept whatever contamination is present in the airflow. This short time operation severely limits the validity of component tests, and air contamination calls into question any propulsion measurements.

In this paper we examine a new approach to the design of a hypersonic facility. This approach leads to the possibility of long run times with properly constituted air (no significant contamination) at static temperatures and pressures characteristic of flight conditions. The basic concept is to maintain the air at moderate temperature but at ultrahigh pressure in the plenum, generating a cold, high-density flow at the throat. After an initial expansion to achieve supersonic flow, additional energy is radiatively coupled into the air as it expands through the nozzle, further accelerating it while simultaneously increasing the enthalpy and entropy. A final expansion to high Mach number brings the flow to the test conditions. With this approach, the air temperature is maintained low throughout the expansion so that thermally induced reactions and throat erosion are minimized.

An important aspect of this approach is that the ultrahigh pressure air in the plenum region has very high density and can no longer be treated as an ideal gas. The associated real gas effects cause the enthalpy to become pressure dependent, and so very high enthalpies can be achieved at modest temperatures. In addition, the speed of sound increases significantly, reaching values more typical of the speed of sound in liquid than in gas-phase air. As a consequence, the kinetic energy of the fluid passing through the throat at Mach 1 is much higher than would be possible for an ideal gas at a similar temperature.

A feature of this approach is that many parameters may be varied to achieve the desired flow. For example, the absorption of the air depends on its density, temperature, and pressure, as well as on the wavelength of the particular radiative source chosen. A change in the absorption will affect the length of the tunnel, which directly impacts the time the air spends at high temperature and, thus, the chemical dynamics, and so the choice of the wavelength can be optimized for the minimization of oxides of nitrogen. Other variables include the plenum pressure, the plenum temperature, the expansion profile, and the energy addition profile. More flexibility may be achieved by using multiple radiation sources, each optimized for a particular portion of the flow. A practical limit for the run time will be determined by the volume of high-pressure air that can be contained and the total stored energy of the radiative source. Run times in excess of 0.1 s are the goal of this approach.

Technical Approach

Overview

A convenient way of viewing the operation of such a facility is with the help of a Mollier diagram (Fig. 1). In this diagram, the

Received Aug. 10, 1994; revision received Jan. 20, 1995; accepted for publication Feb. 14, 1995.

*Professor, Department of Mechanical and Aerospace Engineering. Senior Member AIAA.
†Chairman, Department of Mechanical and Aerospace Engineering.
‡Research Scientist, Department of Mechanical and Aerospace Engineering. Member AIAA.
§Research Scientist, Department of Mechanical and Aerospace Engineering.
¶Graduate Student, Department of Mechanical and Aerospace Engineering.
‖Professor Emeritus, Department of Mechanical and Aerospace Engineering. Fellow AIAA.
**Graduate Student, Physics Department.
††Graduate Student, Applied Physics Department.

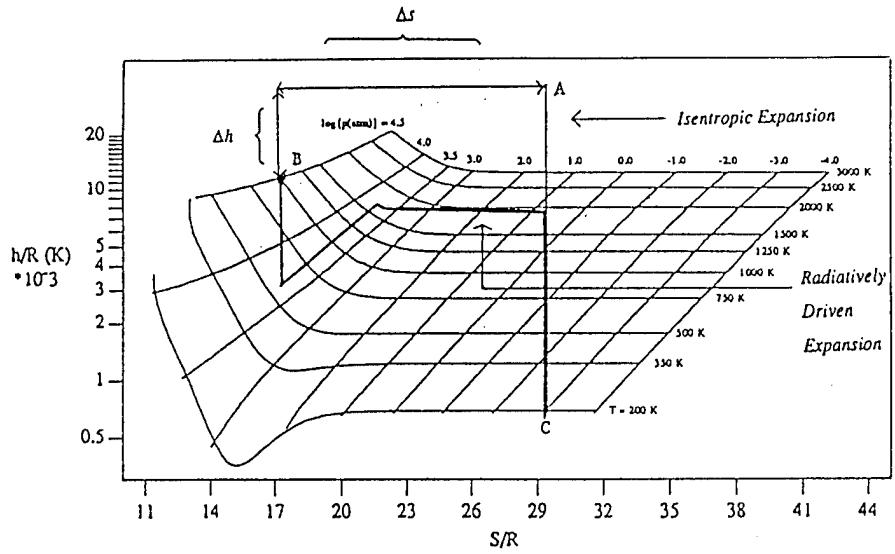

Fig. 1 Concept definition: thermodynamic comparison of wind-tunnel philosophies.

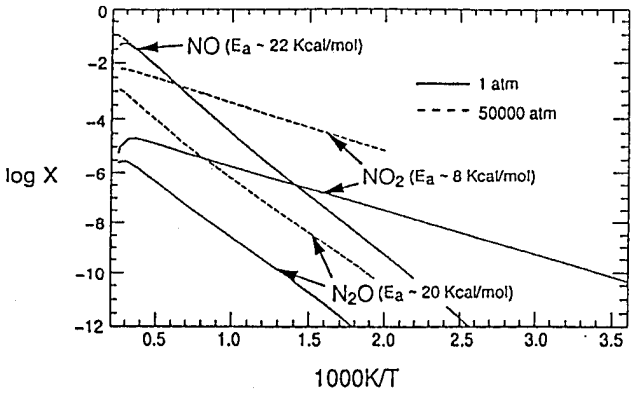

Fig. 2 Equilibrium mole fractions of NO, NO_2, and N_2O in air at 1 and 50,000 atm. For 1 atm, the ideal gas equation of state was applied, and for 50 atm, the Becker–Kistiakowsky–Wilson equation of state was assumed.[1]

enthalpy is plotted vs the entropy. For a conventional wind-tunnel facility, the expansion is assumed to be isentropic, and so the static temperature and pressure and the Mach number in the test chamber mandate a unique temperature and pressure for the gas in the plenum. For example, for a Mach 16 flow with a static temperature of 200 K and a static pressure of 10^{-3} atm (point C on the diagram), the plenum must be held at a temperature of 6300 K and at a pressure of 4000 atm (point A). Clearly, at this temperature, air is highly dissociated, and severe problems with containment and throat erosion occur. In contrast, the radiatively driven wind tunnel begins with a plenum pressure on the order of 30,000 atm but a plenum temperature on the order of 1000 K. The point on the Mollier diagram (point B) associated with this initial condition corresponds to significantly lower entropy and lower enthalpy than that of the isentropic wind tunnel. That remaining enthalpy and entropy are then added downstream of the throat using the radiative source.

Chemistry is an important consideration in the design of the radiatively driven hypersonic facility concept. In the ideal case, the temperatures will be kept low enough so that the chemical kinetics can be ignored. In reality, however, there are two regimes in which chemical kinetics must be taken into account. The first is in the ultra-high-pressure plenum, where even at modest temperatures the formation of polyatomic molecules that have lower specific volume is favored. This effect is illustrated in Fig. 2. If equilibrium codes are extrapolated to 50,000 atm at 1000 K, the predicted equilibrium mole fraction of NO_2 increases by two orders of magnitude above its one atmosphere equilibrium concentration. The mole fraction of NO, on the other hand, is unaffected since it is a diatomic molecule and occupies the same molar volume as oxygen and nitrogen, which are both diatomic. At temperatures on the order of 1500 K or below, the rate of formation of those species is very slow, even at high pressure, and so a facility pulsed for times on the order of a second or less may never reach chemical equilibrium in the plenum.

The second regime of concern is in the region of heat addition where the temperatures increase substantially, and the formation rate of superequilibrium species is nonnegligible. Since the flow is moving at high speed (several kilometers/second), the residence time of the molecules in the high temperature regime is relatively short (milliseconds), and so the kinetic rate of formation of various molecular species becomes an important parameter. In particular, it is important to realize that the slow kinetic rate of formation of the nitric oxide molecule may suppress the nitric oxide concentrations for short times even though the temperature may be high.

One can generate an estimate of the temperature at which the additional enthalpy must be added downstream by recognizing that the total enthalpy (kinetic energy plus static enthalpy) and entropy are determined by the desired test conditions. Therefore, we can identify an enthalpy deficit Δh, which is the difference between the total enthalpy in the test chamber and the enthalpy in the plenum, and an entropy deficit Δs, which is the difference between the entropy of the gas in the test chamber and the entropy in the plenum. In the conventional isentropic facility, the enthalpy and entropy deficits are zero. Assuming an isentropic expansion, the total enthalpy in the test chamber is equal to the plenum enthalpy in the conventional facility, and so the enthalpy deficit is just the enthalpy difference between the plenum enthalpy of the conventional wind tunnel and the plenum enthalpy of the radiatively driven wind tunnel, as shown in Fig. 1. Similarly, the entropy deficit is the difference in plenum entropies as shown in the figure. When energy is added downstream of the throat, the ratio of these two deficits ($\Delta h/\Delta s$) gives an "effective" temperature T_e. This is the effective temperature at which the additional enthalpy must be introduced downstream of the throat to achieve the proper entropy.

To minimize the formation of oxides of nitrogen and radicals in the nozzle section, it is desirable to keep this effective temperature as low as possible. This is accomplished by either decreasing Δh (increasing the enthalpy in the plenum) or increasing Δs (decreasing the entropy in the plenum). From Fig. 1 it is apparent that increasing the enthalpy in the plenum can be achieved by increasing the temperature or by increasing the pressure. Decreasing the entropy is accomplished by increasing the pressure or by decreasing the temperature. It is evident that high pressure is needed to keep the effective temperature low. Figure 3 shows the effective temperature as a function of plenum pressure for various plenum temperatures needed to achieve a Mach 16 flow at 200 K and 10^{-3} atm.

Table 1 Compressibility factor constants

$K(1) = 6.243238 \times 10^{-2}$	$K(12) = -7.271550 \times 10^{-4}$	$K(23) = -8.451945 \times 10^{-2}$
$K(2) = 1.272148 \times 10^{-1}$	$K(13) = -4.524547 \times 10^{-3}$	$K(24) = -3.409313 \times 10^{-3}$
$K(3) = -9.363323 \times 10^{-1}$	$K(14) = 1.304687 \times 10^{-3}$	$K(25) = -1.951270 \times 10^{-3}$
$K(4) = 7.018441 \times 10^{-1}$	$K(15) = -2.221651 \times 10^{-4}$	$K(26) = 4.938999 \times 10^{-5}$
$K(5) = -3.516090 \times 10^{-1}$	$K(16) = -1.981405 \times 10^{-3}$	$K(27) = -4.932646 \times 10^{-5}$
$K(6) = 5.645003 \times 10^{-2}$	$K(17) = 5.975740 \times 10^{-5}$	$K(28) = 8.856666 \times 10^{-7}$
$K(7) = 2.995615 \times 10^{-2}$	$K(18) = -3.641353 \times 10^{-6}$	$K(29) = 5.347880 \times 10^{-8}$
$K(8) = -3.181744 \times 10^{-2}$	$K(19) = 8.413648 \times 10^{-6}$	$K(30) = -5.934206 \times 10^{-8}$
$K(9) = -1.682111 \times 10^{-2}$	$K(20) = -9.828689 \times 10^{-9}$	$K(31) = -9.068133 \times 10^{-9}$
$K(10) = 1.602041$	$K(21) = -1.576831$	$K(32) = 1.618224 \times 10^{-9}$
$K(11) = -1.099967 \times 10^{-3}$	$K(22) = 4.007290 \times 10^{-2}$	$K(33) = -3.320448 \times 10^{-10}$

$$\beta(\tau) = \sum_{i=1}^{6} K(i)\tau^{i-1} \quad \text{and} \quad \lambda = 0.0588$$

ρ and τ are defined in terms of the critical values for the substance to be modeled:

$$r = \frac{RT_c\rho}{P_c} \quad \text{and} \quad \tau = \frac{T_c}{T}$$

where the critical parameters for air are approximated as

$T_c = 132.5$ K $\qquad P_c = 3.77$ MPa $\qquad \rho_c = 343.3$ kg/m^3

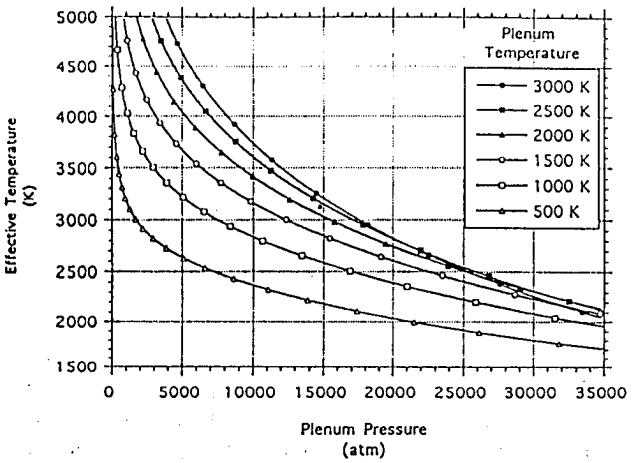

Fig. 3 Effective temperature vs plenum pressure for various plenum temperatures.

Balanced against this effective temperature are the maximum temperature reached in the expansion and the temperature in the plenum. In general, it is these temperatures and the time over which the flow is at these temperatures that determine the concentration of nitric oxide in the test region. Since the effective temperature is an average temperature at which the energy is added, if a significant amount of energy is added below the effective temperature, then an approximately equal amount must be added at a temperature higher than the effective temperature to achieve the proper test conditions. The maximum heating rate downstream of the throat is at constant pressure, since an increase in pressure will cause the flow to choke. Thus, to minimize the peak temperature, the flow should be heated isobarically until it reaches a temperature somewhat higher than the effective temperature, and then the remainder of the energy added. In the models presented here, we have chosen an initial expansion to Mach 2 before energy is added to avoid instabilities near Mach 1. Because of real gas effects, in the initial constant pressure heating region the Mach number does not drop significantly, even though the temperature increases by a factor of 3 or more.

Flow Model

A more accurate description of the operation of the wind tunnel can be developed using a one-dimensional real gas model. The governing equations are the continuity, momentum, and energy equations that are derived from a control volume analysis with heat input $\dot{q}$, expressed in joules per unit mass per unit length,

$$\rho u\frac{dA}{dx} + \rho\frac{du}{dx}A + \frac{d\rho}{dx}uA = 0 \tag{1}$$

$$\left(\frac{\partial P}{\partial \rho}\right)_T\frac{d\rho}{dx} + \left(\frac{\partial P}{dT}\right)_\rho\frac{dT}{dx} = -\rho u\frac{du}{dx} \tag{2}$$

$$\left(\frac{\partial h}{\partial \rho}\right)_T\frac{d\rho}{dx} + \left(\frac{\partial h}{\partial T}\right)_\rho\frac{dT}{dx} + u\frac{du}{dx} = \frac{\dot{q}}{\rho uA} \tag{3}$$

where ρ is the density, h is the specific enthalpy, and u is the velocity. The equation of state is[2]

$$P = Z(\rho, T)\rho RT \tag{4}$$

where the compressibility factor is given as

$$\begin{aligned} Z = {} & 1 + r\beta(\tau) + r^2\sum_{i=7}^{10}K(i)\tau^{i-7} + r^3\sum_{i=11}^{13}K(i)\tau^{i-11} \\ & + r^4K(14)\tau + r^5[K(15)\tau^2 + K(16)\tau^3] \\ & \times r^6K(17)\tau^2 + r^7[K(18)\tau^2 + K(19)\tau^3] \\ & + r^8K(20)\tau^3 \\ & + \begin{bmatrix} r^2[K(21)\tau^3 + K(22)\tau^4] \\ + r^4[K(23)\tau^3 + K(24)\tau^5] \\ + r^6[K(25)\tau^3 + K(26)\tau^4] \\ + r^8[K(27)\tau^3 + K(28)\tau^5] \\ + r^{10}[K(29)\tau^3 + K(30)\tau^4] \\ + r^{12}[K(31)\tau^3 + K(32)\tau^4 + K(33)\tau^5] \end{bmatrix} \cdot e^{-\lambda r^2} \end{aligned} \tag{5}$$

with r being a dimensionless density based on the critical temperature T_c and the critical pressure P_c,

$$r = \rho\frac{RT_c}{P_c} \tag{6}$$

and τ being a dimensionless temperature,

$$\tau = \frac{T_c}{T} \tag{7}$$

The constants $K(i)$ are listed in Table 1. To find the other thermodynamic state variables, the ideal gas specific heat, $c_v^0(T)$, is used to

find the low-density ($\rho = \rho_\epsilon$) (ideal gas) conditions at temperature T, and then the real gas equation is used to integrate at constant T to the desired density.[2] Therefore, for enthalpy and entropy,

$$\frac{h - h^0}{RT_c} = \int_{r_\epsilon}^{r} \frac{1}{r}\left(\frac{\partial Z}{\partial \tau}\right)_r \mathrm{d}r + \frac{(z-1)}{\tau} \tag{8}$$

and

$$\frac{s - s^0}{R} = -\ell_n\left(\frac{\rho}{\rho_\epsilon}\right) + \int_{r_\epsilon}^{r} \frac{\tau}{r}\left(\frac{\partial Z}{\partial \tau}\right)_r \mathrm{d}r - \int_{r_\epsilon}^{r} \frac{1}{r}(Z-1)\,\mathrm{d}r \tag{9}$$

where $r_\epsilon = \rho_\epsilon(RT_c/P_c)$ is effectively zero for the lower limits of the integrals, and h^0 contains the low-density specific enthalpies of oxygen and nitrogen and contains the low-density specific entropies of oxygen and nitrogen plus the entropy of mixing.

This model has been found to give an accurate reproduction of the Arnold Engineering and Development Center (AEDC) Mollier diagram that is derived from tabulated data, and it is consistent with similar real gas models published by the Soviet Bureau of Standards.[3-5] This equation of state is solved using a finite difference solution to generate an aerodynamic model to describe the flow evolution with heating in the nozzle section. The model does not account for dissociation or high temperature and has been developed based on nitrogen data only up to 10,000 atm pressure at temperatures between 50 and 1200 K. Extrapolations to higher pressure and temperature are smooth but have not been experimentally verified. The application of this model to air rather than nitrogen involves a single substance approximation for the critical pressure and temperature. To our knowledge there are no experimental data for air above 4550 atm.[6]

This model was tested in several manners. First, with no energy addition and at constant area, calculated values of the density, temperature, and velocity were checked to confirm that these quantities remained constant throughout the flow. A second check was done modeling a diverging conical profile with initial conditions corresponding to the Mach number just greater than 1 and no energy addition. Calculated ρ/ρ^*, T/T^*, P/P^*, and A/A^* profiles produced by the model were compared with tabulated solutions for an isentropic expansion. There was no perceptible deviation from the isentropic case. A third verification used the exactly solvable problem of energy addition into a flow with a constant cross-sectional area. The exact solution in this case is given by the expression

$$\mathrm{d}h = \left[1 - \frac{u^2\alpha}{c_p(1-M^2)}\right]\mathrm{d}s \tag{10}$$

where α is the isobaric expansion coefficient,

$$\alpha = \frac{1}{v}\left(\frac{\partial v}{\partial T}\right)_p \tag{11}$$

and v is the specific volume $(1/\rho)$. Both α and the specific heat c_p were calculated numerically, and the ratio $(\mathrm{d}h/\mathrm{d}x)/(\mathrm{d}s/\mathrm{d}x)$ was normalized by Eq. (10) and checked to be sure that the value remained unity as the flow evolved down the constant area duct. The result was accurate to one part in 10^6, independent of ρ, T, v, and $\dot{q}$ for appropriately small step sizes. The computation uses as an independent variable either the area profile $A(x)$, the pressure profile $p(x)$, or the temperature profile $T(x)$. The energy deposition rate $\dot{q}(x)$ can either be specified, or it can be derived from the absorption characteristics of the air, which are modeled as a function of temperature and pressure.

Energy Addition

The performance of the wind tunnel depends on both the plenum conditions and on the mechanism for energy addition. Using current technology, the maximum plenum pressure achievable is estimated to be between 20,000 and 30,000 atm. Energy must be added to the moving flow, and so radiative coupling is an obvious approach. This coupling must be accomplished via absorptive energy transitions that occur in air. The very high pressure of the air just downstream of the throat will lead to significant pressure dependence

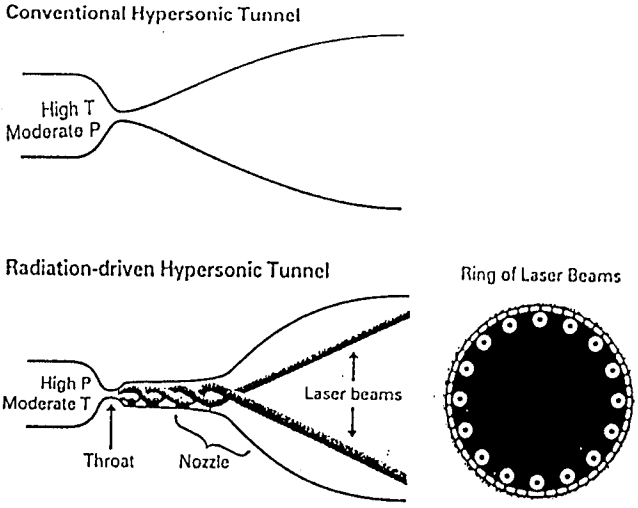

Fig. 4 Schematic comparison of wind-tunnel philosophies.

(both pressure narrowing and pressure broadening) of absorption features, and at these high pressures, pressure-induced absorption phenomena are often dominant. Transitions occurring in the infrared region are accessible to various high-power lasers, and those in the microwave region can be pumped by high-power gyrotron devices. Of particular interest are pressure-induced transitions in oxygen in the near infrared that overlap diode lasers and diode-pumped, solid-state lasers; CO_2 transitions that overlap hydrogen fluoride (HF) and reactor pumped xenon laser lines; H_2O transitions that overlap the chemical oxygen iodine laser (COIL); and the oxygen microwave transition at 60 GHz. Other transitions to be explored include H_2O and CO_2 lines that overlap CO_2 and CO lasers and pressure-induced oxygen and nitrogen transitions throughout the infrared. Ultraviolet transitions, particularly those in oxygen, might also be explored with high-power light sources and, possibly, with ultraviolet lasers.

As a test case, the possibility of adding energy optically with high-power HF lasers was studied. Although the calculation is one dimensional, a possible tunnel geometry is sketched in Fig. 4. The lasers are assumed to enter the tunnel from downstream, passing through the test section and into the nozzle. They are arranged in a ring so as not to interfere with the model. Since most of the absorption occurs where the air is at high pressure, this configuration has the potential of efficiently coupling energy into the flow just downstream of the throat. To compute the flow, an initial guess of the energy deposition parameter $\dot{q}$ through the nozzle is given, and the model is integrated in the forward direction to solve for the air density and temperature through the expansion, and then in the backward direction (from the test section back toward the throat) to give a second iteration on the energy addition profile based on the energy absorbed by the air at the computed temperature and density. This procedure is carried out repeatedly until convergence is achieved. Following convergence, the energy addition rate profile is consistent with the absorptivity profile of the expanding airstream.

Although the thermodynamic properties of the gas appear to be good approximations to the actual thermodynamic state of air over these ranges of pressure and temperature, the absorption constant is only a crude estimate. In the example worked here, the high-power HF lasers are assumed to be operating on a single transition near 2.76 μ (3623 cm^{-1}). Absorption occurs through the small amount of CO_2 that is present in air and reflects the upper atmospheric mole fraction ratio of 330 parts/million. The absorption is directly into a bending/asymmetric stretch (021) combination band, and absorption data are taken from the HITRAN database, extrapolated to high pressure using conventional pressure broadening.[7] Since pressure narrowing effects are ignored, the values that are used only serve to illustrate this approach to energy addition and cannot be interpreted quantitatively. Figure 5 shows the absorption profile in the vicinity of the HF line at a pressure of 1000 atm. To accommodate our uncertainty in the absorption line shape and magnitude, a pressure-dependent absorption constant equivalent to one-half of that shown on the figure for the $P_2(4)$ line was used for the calculation.

Table 2 Computed gases

Stagnation conditions	Cases 1 and 2
Temperature, K	1500
Pressure, atm	2.51×10^4
Density, kg/m^3	1.12×10^3
Enthalpy, J/kg	3.54×10^6
Entropy, J/kg · K	5.56×10^3
Flow rate, kg/s	79.0
Throat conditions (Mach 1)	
Velocity, m/s	1.86×10^3
Temperature, K	1080
Density, kg/m^3	8.17×10^2
Area, m^2	5.19×10^{-5}
Pressure, atm	8.33×10^3

Exit conditions	Case 1	Case 2
Mach no.	14.5	15.0
Velocity, m/s	4.05×10^3	4.25×10^3
Temperature, K	194	201
Density, kg/m^3	1.82×10^{-3}	1.76×10^{-3}
Area, m^2	10.7	10.6
Pressure, atm	1.00×10^{-3}	1.00×10^{-3}
Static enthalpy, J/kg	1.90×10^5	1.90×10^5
Total enthalpy, J/kg	8.40×10^6	9.22×10^6
Entropy, J/kg · K	8.40×10^3	8.44×10^3
Equivalent isentropic plenum conditions (from AEDC Mollier diagram)		
Temperature, K	5550	5800
Pressure, atm	2.24×10^3	2.82×10^3

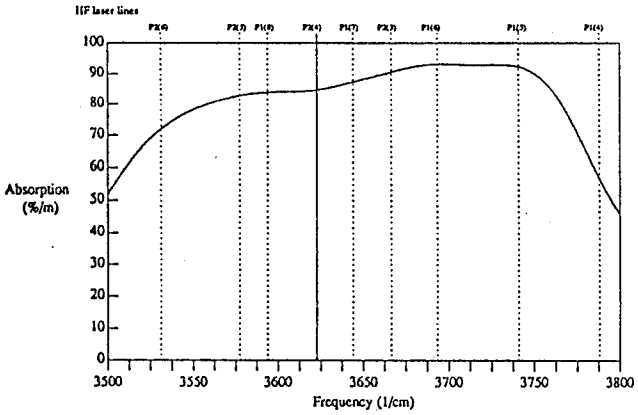

Fig. 5 CO_2 absorption (percent per meter) for air at 1000 atm and 1000 K. Vertical lines correspond to HF laser lines.

Two examples are given to demonstrate the effect of different expansions. Both cases begin with the same plenum pressure, 25,120 atm, and temperature, 1500 K, and are expanded to roughly 200 K and 10^{-3} atm. Mach numbers of 14.5 and 15.0 are achieved by cases 1 and 2, respectively. The stagnation conditions, throat conditions, and conditions in the test section for the computed cases are shown in Table 2. The constraint applied for the calculation was initial energy addition at constant pressure, followed by isothermal energy addition, and a final expansion to the test cell that has approximately a 3-m diameter. In the first case, the flow is heated at constant pressure to 2000 K and then heated at constant temperature. Since the code is one dimensional, the length and shape of the final expansion are arbitrary. The shape of the final expansion is chosen here to produce a smooth pressure drop to 10^{-3} atm pressure, and the length of the tunnel is chosen to be 40 m. In the second case, the flow is heated at constant pressure up to 2500 K and then heated at constant temperature until the proper entropy is reached. The initial conditions for the energy addition portion of the computation begin at Mach 2 in both cases, and so the flow passes through the throat and expands to Mach 2 before heat addition begins. In both cases, the optical energy is fully absorbed downstream of the Mach 2 position by allowing sufficient separation between the nozzle location and the energy addition regime, and so there is no truncation error associated with these initial conditions.

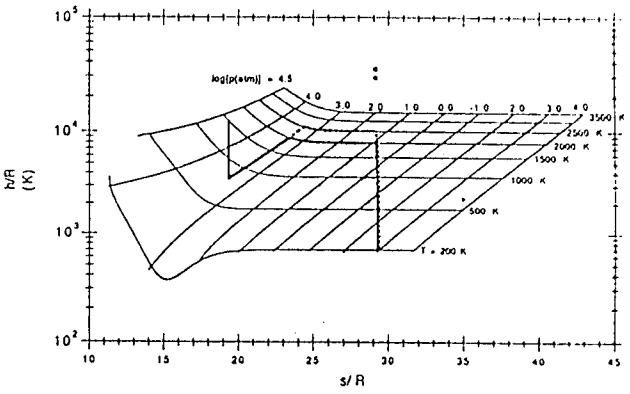

Fig. 6 Mollier diagram for cases 1 (2000 K—solid line, solid dot) and 2 (2500 K—dotted line, open dot).

Figure 6 shows the trajectories of cases 1 and 2 on the Mollier diagram. The points at the top of the diagram show the initial conditions for an isentropic expansion to achieve the same test conditions. These numbers are taken from the AEDC Mollier diagram since our model is not designed for exceedingly high temperature.

Figures 7a–7f show the pressure, temperature, tunnel radius, Mach number, flow velocity, and heating profile as a function of the axial distance downstream for these two cases. It is particularly striking to note the large change in tunnel radius as a function of axial distance. Figures 8a and 8b show an expanded view of the radius and the heating profile over the first few meters. Because of the very high density of the fluid at the throat, the radius at that location is less than 5 mm. Apparent discontinuities in these curves are due to discontinuous changes in the modeled expansion profiles or energy addition constraints. As the flow proceeds downstream, energy addition occurs primarily over the first few meters, after which the secondary expansion increases the radius to on the order of 1.7 m. The fluid flow characteristics at the throat are shown in Table 2. Note that the velocity at the throat is 1,860 m/s. This sonic speed would correspond to an "ideal gas" at a temperature in excess of 8000 K, whereas the flow temperature is actually 1080 K.

In case 2, significantly more energy is coupled into the flow since it is heated to 2500 K rather than 2000 K before the isothermal energy addition begins. This is reflected both in the test conditions and in the effective temperatures. In case 1, the effective temperature is 1740 K, the flow velocity in the test section is 4.05 km/s, and the static temperature is 194 K. For case 2, the effective temperature is 1970 K, the flow velocity is 4.25 km/s, and the temperature in the test section is 201 K.

Flow Chemistry

An important design goal for this wind-tunnel facility is to match the molecular concentrations that are found at the flight altitudes simulated. Particular difficulty arises with regard to the molecular concentration of nitric oxide, since that species is formed in abundance at high temperature and tends to freeze into the flow. Nitric oxide concentrations in the upper atmosphere range from on the order of 50 parts/billion up to 80 km (260,000 ft) and then increase to a maximum of approximately 200 parts/million at 110 km (360,000 ft).[8] These mole fractions correspond to equilibrium temperatures ranging from approximately 600 to 1200 K, according to the equilibrium diagram shown in Fig. 2. An important feature of this facility is that, even though the air must reach temperatures higher than these numbers, the time at which it remains at those temperatures is short, and therefore the nitric oxide concentrations are significantly suppressed below their equilibrium levels. This occurs both in the plenum where, even though the pressure is very high, the temperature is low, and so the kinetic formation rate of nitric oxide is on the order of seconds, and in the expansion, where the temperatures are higher but the times for formation are only on the order of milliseconds.

To compute the NO concentrations, we have applied an elementary chemical kinetic model based on 23 principal air reactions and the real gas Becker–Kistiakowsky–Wilson equation of state. These

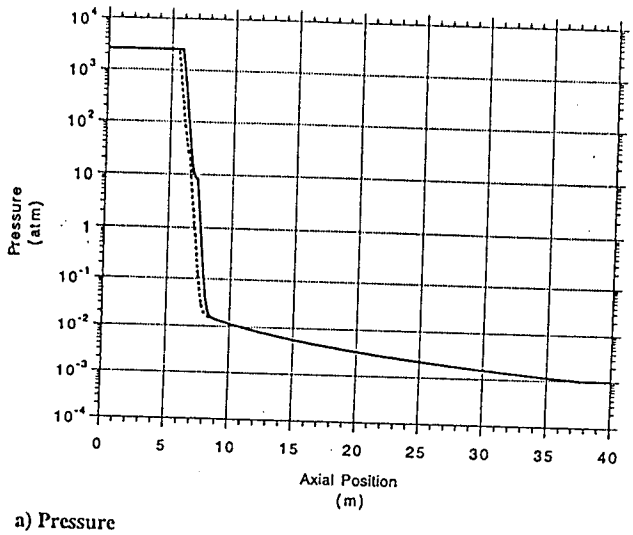

a) Pressure

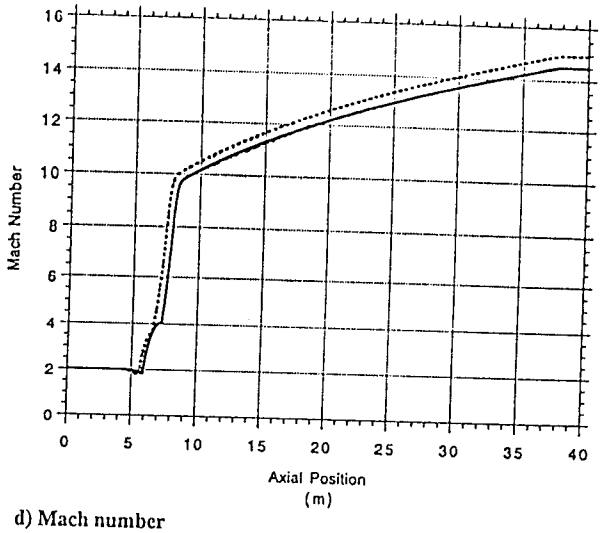

d) Mach number

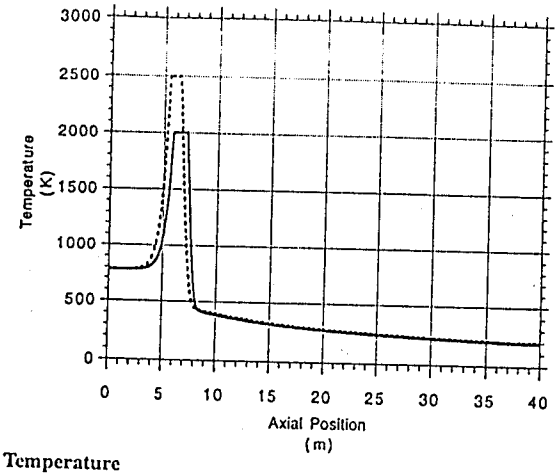

b) Temperature

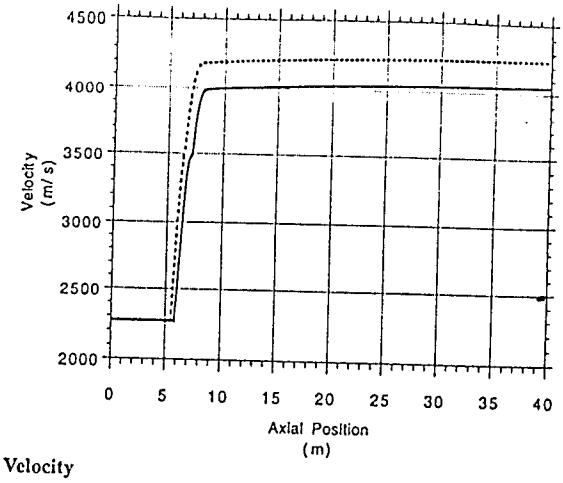

c) Velocity

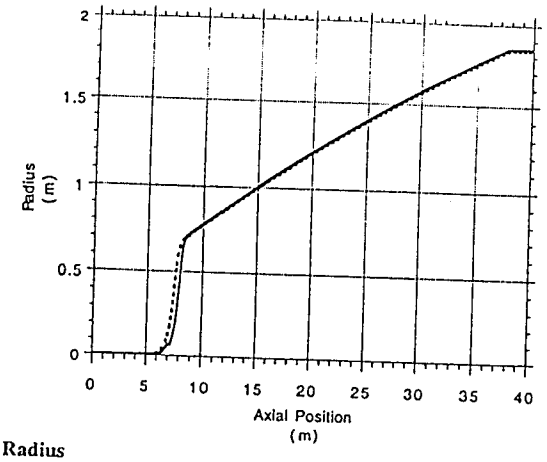

e) Radius

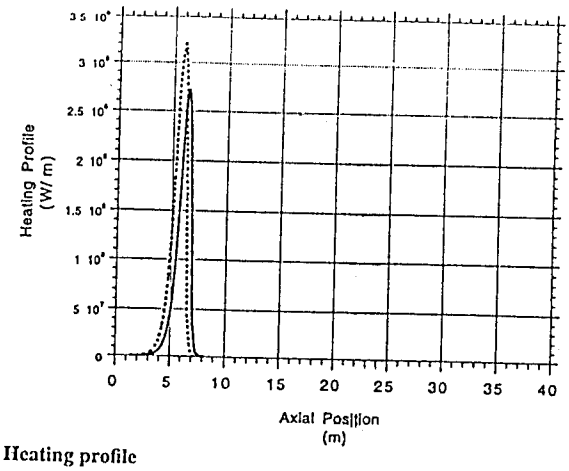

f) Heating profile

Fig. 7 Tunnel parameters for cases 1 (2000 K—solid line) and 2 (2500 K—dotted line).

reactions and the pressure-dependent rates are given in Table 3. Nitric oxide, oxygen radical, and NO_2 concentrations for the two cases discussed earlier are shown in Figs. 9 and 10. It is important to note that the equilibrium molar concentration for nitric oxide at 2000 K is approximately 10^{-2} (1%). Here we see that in case 1 the formation of nitric oxide has been dramatically suppressed by the slow chemical formation rates. In case 2, however, the flow is maintained at 2500 K for a relatively long period of time, and the nitric oxide concentration comes close to its equilibrium value. These curves suggest that various different scenarios for energy addition will have a significant impact on the level of nitric oxide formed. The concentrations of other nonequilibrium species are lower than NO but cannot be neglected.

In this model, the time delay between the excitation of the CO_2 molecule and the deposition of energy into the kinetic motion of the flow is modeled assuming a single vibrational temperature. Although the exact mechanisms for this energy transfer remain to be explored, it is expected that the CO_2 molecule will rapidly transfer its energy to nitrogen by exciting the vibrational mode of the nitrogen molecule. At low pressure, vibrationally excited nitrogen has a very long relaxation time. At high pressures, however, nitrogen rapidly transfers its excitation to oxygen, which is rapidly thermalized. Accurate modeling of both the collisional energy transfer from CO_2 to nitrogen and the nitrogen relaxation mechanism will be important since many photons must be transferred to each CO_2 molecule to achieve the required heating rates. The

Table 3 High-temperature air reaction mechanism[a]

	Reaction[b]	A	n	E	A_0	n_0	E_0	a	b
1	$O_2(+M) = 2O(+M)$	0.15×10^{12}	0.0	118,000.0	0.98×10^{25}	−2.5	118,000.0	—	—
2	$O + O_2(+M) = O_3(+M)$	0.17×10^{13}	0.0	—0.0	0.18×10^{22}	−2.8	—0.0	0.65	—
3	$O + O_3 = 2O_2$	0.12×10^{14}	0.0	—4.5	—	—	—	—	—
4	$CO + O + M = CO_2 + M$	—	—	—	0.25×10^{14}	0.0	−4,541.0	—	—
5	$CO + O_2 = CO_2 + O$	0.25×10^{13}	0.0	47,690.0	—	—	—	—	—
6	$NO(+M) = N + O(+M)$	0.15×10^{12}	0.0	148,000.0	0.15×10^{16}	0.0	148,400.0	—	—
7	$NO + O(+M) = NO_2(+M)$	0.13×10^{16}	−0.75	0.0	0.47×10^{25}	−2.87	1,550.0	0.95	1.0×10^{-4}
8	$NO + O = O_2 + N$	0.18×10^{10}	1.0	38,760.0	—	—	—	—	—
9	$2NO = N_2 + O_2$	0.13×10^{15}	0.0	75,630.0	—	—	—	—	—
10	$NO_2 + O = O_2 + NO$	0.39×10^{13}	0.0	−238.4	—	—	—	—	—
11	$NO_2 + O(+M) = NO_3(+M)$	0.13×10^{14}	0.0	0.0	0.15×10^{29}	−4.08	1,467.0	0.79	2.5×10^{-4}
12	$NO_2 + NO = N_2O + O_2$	0.10×10^{13}	0.0	60,000.0	—	—	—	—	—
13	$2NO_2 = NO_3 + NO$	0.96×10^{10}	0.73	20,920.0	—	—	—	—	—
14	$2NO_2 = 2NO + O_2$	0.16×10^{13}	0.0	26,120.0	—	—	—	—	—
15	$N_2O(+M) = N_2 + O(+M)$	0.13×10^{12}	0.0	59,610.0	0.72×10^{18}	−0.73	62,790.0	1.17	1.25×10^{-4}
16	$N_2O + O = N_2 + O_2$	0.10×10^{15}	0.0	28,020.0	—	—	—	—	—
17	$N_2O + O = 2NO$	0.66×10^{14}	0.0	26,630.0	—	—	—	—	—
18	$N_2O + NO = N_2 + NO_2$	0.10×10^{15}	0.0	49,675.0	—	—	—	—	—
19	$N + NO = N_2 + O$	0.33×10^{13}	0.3	0.0	—	—	—	—	—
20	$N + N_2O = N_2 + NO$	0.10×10^{14}	0.0	19,870.0	—	—	—	—	—
21	$N + NO_2 = 2NO$	0.40×10^{13}	0.0	0.0	—	—	—	—	—
22	$N + NO_2 = N_2O + O$	0.50×10^{13}	0.0	0.0	—	—	—	—	—
23	$N + NO_2 = N_2 + O_2$	0.10×10^{13}	0.0	0.0	—	—	—	—	—

[a]Units are cm^3-mole-s-cal, $k = AT^n \exp(-E_a/RT)$.
[b]For pressure-dependent reactions with the total concentration, M listed in parentheses, fall-off behavior is included as follows:

$$k = \left\{ \frac{k_0 k_\infty}{k_0 + (k_\infty/[M])} \right\} \times F$$

$$\log F = \frac{\log F_c}{\{1 + [\log(k_0 \times [M]/k_\infty)]^2\}}$$

$$k_0 = A_0 T^{n_0} \exp(-E_0/RT)$$

$$k_\infty = AT^n \exp(-E/RT)$$

$$F_c = a - bT$$

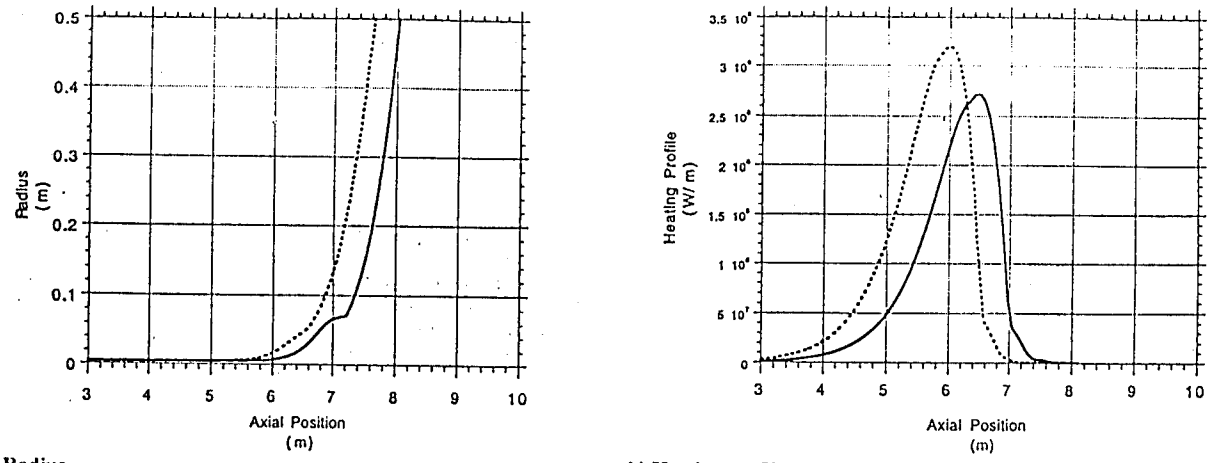

a) Radius b) Heating profile

Fig. 8 Expanded scale wind-tunnel parameters for cases 1 (2000 K—solid line) and 2 (2500 K—dotted line).

scale of this energy deposition problem can be better appreciated by realizing that the enthalpy deficits in cases 1 and 2 are 4.9 and 5.7 million J/kg, respectively. This corresponds to approximately 10,000 photons per CO_2 molecule, all of which must be absorbed in a few milliseconds, and so collisional transfer rates shorter than 0.1 μs are required. In a large-scale facility such as this, a flow rate on the order of 80 kg/s will be necessary. Thus, a total energy deposition rate of 400–450 MW must be achieved over the run time of the tunnel. This involves a significant scaling of candidate laser sources and the use of multiple lasers. Tunnel operation for 0.1 s will require a total energy of 50 MJ to be deposited into the flow. By comparison, this is approximately the amount of energy stored in 20 gal of gasoline and is well within the current total energy capability of existing high-power hydrogen fluoride/deuterium fluoride (HF/DF) lasers.

Alternate Approaches

The use of an HF laser to achieve energy addition via a CO_2 transition has the advantage that very high-power HF and DF lasers have already been developed through Department of Defense support. For example, the MIRACL laser currently is capable of operating at power levels in excess of 1×10^6 W. Further scaling of that laser to power levels on the order of 300×10^6 W will constitute

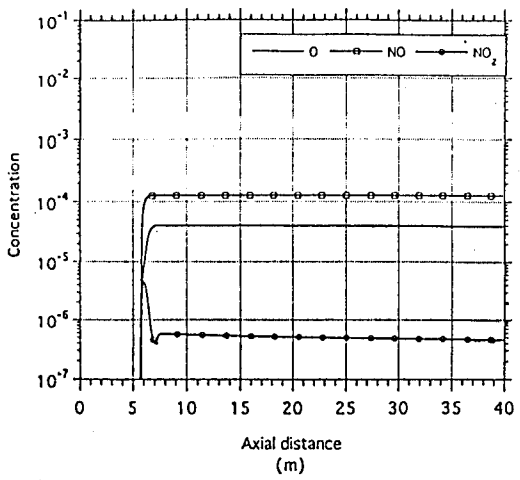

Fig. 9 Nonequilibrium concentrations for case 1.

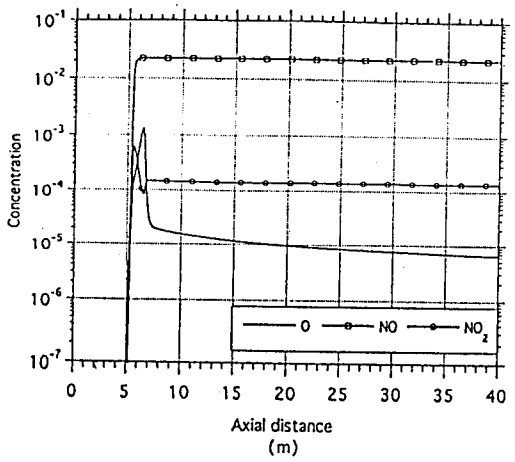

Fig. 10 Nonequilibrium concentrations for case 2.

a major engineering challenge. Other candidate laser sources for energy transfer include the nuclear reactor pumped Xe laser operating at 2.76 μ, the free electron laser with its variable frequency operation, the chemical oxygen iodine laser that runs at 1.4 μ, high efficiency diode lasers operating in the near infrared, the carbon dioxide laser in the 10-μ region, and the carbon monoxide laser in the 5-μ region. In all cases, significant scale-ups will be required to generate enough power to drive a full-scale facility.

Other aspects that must be examined include optical propagation through the high-temperature air and the possible interaction of high-power laser beams with the walls. Of particular concern is electric-field-generated breakdown in the energy-addition region of the flow. Although this occurs at very high intensities for laser radiation, the variation of breakdown as a function of pressure is of concern. It is, perhaps, encouraging to note that the breakdown threshold reaches a minimum with pressure, which in air at the CO_2 laser wavelength occurs at approximately 20-atm pressure. At pressures higher than that, the breakdown threshold begins to increase since the breakdown dynamics become dominated by collisional processes.[9] Breakdown is also very strongly dependent on the frequency of the electric field, with the breakdown threshold being much higher for high frequency, i.e., near infrared and visible lasers, than for low frequency, i.e., far infrared lasers or microwave devices. Another complexity that will have to be investigated is the interaction of the source radiation field with the two-dimensional flow structure including the boundary layer. The high-temperature boundary layer near the walls will cause the air density to be lower there than in the central portion of the flow. This density variation will lead to an index-of-refraction contour that may be used with the geometry shown in Fig. 4 to help guide the lasers and avoid excess wall heating.

Alternate methods for depositing energy downstream of the throat need to be examined. A particularly attractive approach is to use very high-power microwave gyrotrons to drive molecular oxygen in the vicinity of 60 GHz.[10,11] The very rapid coupling of the oxygen molecule to the translational kinetic modes in air suggests that this approach can potentially be used to deposit large amounts of energy. Microwave gyrotron sources in the megawatt region are currently available, and an increase of power on the order of a factor of 10 can be anticipated in the near future, particularly given that continuous operation may not be required for this facility.

Conclusions

These preliminary examples suggest that a radiatively driven hypersonic air facility may be feasible. Major questions still remain, particularly regarding the effects of transport phenomena at high pressure, the energy-addition mechanism, and the associated chemical kinetics. The basic concept of achieving high enthalpy by using ultrahigh pressure and coupling energy in downstream of the throat does, in principle, lead to a wind-tunnel apparatus in which the air remains cool compared with other approaches. High-pressure plena have been constructed in Russia, and ultrahigh pressures have been achieved in small-scale laboratory devices. Issues relating to gas transport also must be further examined. These include such critical considerations as nozzle erosion, wall cooling, and nonequilibrium phenomena. Although these questions will require significant research to be done in a variety of fields, it is worthwhile to point out that the development of a true air hypersonic test facility will have a major impact on the design and testing of hypersonic vehicles.

Acknowledgments

This work was supported by the Air Force Arnold Engineering Development Center (AEDC) under the supervision of Keith Kushman. The concept was initially formulated in January of 1992 and significantly developed through the undergraduate research efforts of Jeffrey Guest in the spring of 1992 and Douglas Natelson the following year. Additional student support was provided through an Air Force Office of Scientific Research AASERT grant. A series of four workshops held at AEDC, Phillips Laboratory, NASA Langley, and Princeton University served to further establish the technical details and developmental challenges. Particular thanks are given to Marc Costantino of Lawrence Livermore Laboratories, who has contributed his expertise in high-pressure technologies along with his enthusiasm and encouragement. We also recognize the valuable suggestions of our Russian colleagues and greatly appreciate their willingness to share their high-pressure technologies with us.

References

[1]Mader, C. L., *Numerical Modeling of Detonations*, Univ. of California Press, Berkeley, CA, 1979, pp. 412–448.

[2]Reynolds, W. C., *Thermodynamic Properties in SI*, Dept. of Mechanical Engineering, Stanford Univ., Stanford, CA, 1979, pp. 157–159.

[3]Brahinsky, H. S., and Northcutt, D., *Mollier Diagram for Equilibrium Air*, von Kármán Gas Dynamics Facility, Arnold Engineering Development Center, Parthenon Press, Nashville, TN, 1967.

[4]Sychev, V. V., Vasserman, A. A., Kozlov, A. D., Spiridonov, G. A., and Tsymarny, V. A., *Thermodynamic Properties of Air*, Hemisphere, Washington, DC, 1987, pp. 119–199.

[5]Sychev, V. V., Vasserman, A. A., Kozlov, A. D., Spiridonov, G. A., and Tsymarny, V. A., *Thermodynamic Properties of Nitrogen*, Hemisphere, Washington, DC, 1987, pp. 143–236.

[6]Kiyama, R., "The Compressibility of the Air Under Ultra Pressure," *Review of Physical Chemistry of Japan*, Vol. 19, No. 1, 1945, pp. 38–42 (in Japanese).

[7]Rothman, L. W., Gamache, R. R., Goldman, A., Brown, L. R., Toth, R. A., Pickett, H. M., Poynter, R., Flaud, J.-M., Camy-Peyret, C., Barbe, A., Husson, N., Rinsland, C. P., and Smith, M. A. H., "The HITRAN Database: 1986 Edition," *Applied Optics*, Vol. 26, No. 19, 1987, pp. 4058–4097.

[8]Frederick, J. E., and Abrams, R. B., "Model Studies of Nitric Oxide Fluorescence in the Earth's Backscattered Spectrum," *Planetary and Space Science*, Vol. 30, No. 2, 1982, pp. 137–145.

[9]Raizer, Y. P., *Gas Discharge Physics*, Springer–Verlag, Berlin, 1991, p. 154.

[10]Cassidy, P., Boeing Corporation, and Jory, H., Varian Corporation, private communications, 1993.

[11]Mingelgrin, U., Gordon, R. G., Frenkel, L., and Sullivan, T. E., "Microwave Spectrum of Compressed O_2—Foreign Gas Mixtures in the 48-81 GHz Region," *Journal of Chemical Physics*, Vol. 57, No. 7, 1972, pp. 2923–2931.

AIAA 95-2142

ENERGY ADDITION AND THERMALIZATION ISSUES IN A RADIATIVELY-DRIVEN HYPERSONIC WIND TUNNEL

S. Macheret, G. Williams, G. Comas,
C. Meinrenken, W. Lempert, and R. Miles

Dept. of Mechanical & Aerospace Engineering
PRINCETON UNIVERSITY
Princeton, New Jersey 08544 U.S.A.

30th AIAA Thermophysics Conference
June 19-22, 1995/San Diego, CA

ENERGY ADDITION AND THERMALIZATION ISSUES IN A RADIATIVELY-DRIVEN HYPERSONIC WIND TUNNEL

S. Macheret,* G. Williams,** G. Comas,***
C. Meinrenken,+ W. Lempert,++ and R. Miles+++

Department of Mechanical & Aerospace Engineering
PRINCETON UNIVERSITY
Princeton, New Jersey 08544 U.S.A.
609/258-5131

ABSTRACT

We present some of the fundamental spectroscopic and dynamic issues relevant to radiative coupling of large amounts of energy into supersonic flow. The work is motivated by the Radiatively-Driven Hypersonic Wind Tunnel (RDHWT) concept, which has been suggested as a possible path to future hypersonic ground test facilities. The RDHWT relies on ultrahigh plenum pressure, followed by downstream radiative energy addition to achieve high Mach number. In particular, we focus on issues of molecular absorption and collisional thermalization in high pressure air at moderate (1,000-3,000 K) temperatures.

Quantitative models are developed to predict infrared absorption properties of high-pressure air, including spectral line mixing and collision-induced absorption bands. These models are found to agree well with available experimental data. Microwave absorption spectra, including oxygen resonant absorption at 60 GHz, collision-induced absorption, and absorption by free electrons are described, and a simple quantitative model is developed.

The key pathways for vibrational relaxation of infrared energy are identified, potential rate-controlling processes are revealed, and a simple, single vibrational temperature model is developed.

*Research Scientist, Senior Member AIAA
**Graduate Student, Student Member AIAA
***Staff, Student Member ASME
+Graduate Student
++Research Scientist, Member AIAA
+++Professor, Senior Member AIAA

1. INTRODUCTION

The ability to develop hypersonic technology is constrained by the lack of appropriate ground test facilities. The difficulty is easily understood. If high-temperature air in a plenum is expanded isentropically to the desired Mach number, then, to produce air flow at a Mach number exceeding 12 at a static pressure and temperature of 10^{-3} atm and 300 K, respectively, the plenum pressure must exceed 4,000 atm, and plenum temperature must exceed 6,000 K. At this high temperature, air cannot be contained, and, if it could, it would be highly dissociated. For this reason, run times of conventional hypersonic facilities are short (of the order of milliseconds), and the flow in the test section is highly contaminated with NO and radicals.

A new approach aimed at circumventing this fundamental problem has recently been suggested at Princeton.[1] The new concept, called a Radiatively-Driven Hypersonic Wind Tunnel (RDHWT), relies on ultrahigh pressures (20,000-50,000 atm) and moderate temperatures (900-1500 K) in the plenum. This dense air is initially expanded through a nozzle to 4,000-7,000 atm and a Mach number, of say, 2. Since the speed-of-sound in this dense fluid is much higher than that of an ideal gas with the same temperature, the kinetic energy at this point is many times higher than it would be for the corresponding expansion of an ideal gas. Additional energy now must be supplied to the air to achieve the necessary total enthalpy, while continuing expansion and acceleration. The heat addition should also proceed at temperatures such that the entropy reaches that of the desired test section conditions. For the energy addition, radiative sources, such as lasers or microwaves, were suggested in Ref. [1].

By keeping static temperature relatively low at all points of the flow, the RDHWT should be capable of significantly decreasing throat erosion and the production of atypical chemical species, and allow relatively long run times.

While the preliminary modeling results presented in Ref. [1] were encouraging, there are many major issues which have to be considered.

In the present paper, we focus on some of the issues relevant to the physics of energy addition. We discuss fundamental mechanisms of infrared and microwave absorption in high-pressure air, and develop quantitative models which can be compared with the experiments. Pathways of molecular energy transfer and thermalization are considered, and qualitative effects are discussed.

2. INFRARED ABSORPTION IN HIGH-PRESSURE AIR

2.1. Basic mechanisms.

Transmission and absorption of infrared radiation in the atmosphere has been extensively studied over the last few decades. Comprehensive databases, such as the Air Force Geophysics Laboratory compilation, are readily available, as are codes for line-by-line high-resolution computation.[2,3] However, in order to quantitatively evaluate infrared energy addition for the RDHWT, absorption characteristics need to be known for temperatures up to a few thousand Kelvin and pressures up to several thousand atmospheres. The existing standard codes cannot handle this problem adequately, because they do not account for physical phenomena which become very important at high pressures. Let us briefly consider these phenomena.

Line mixing. Widths of pressure-broadened vibrational-rotational lines (typically 0.05-0.08 cm^{-1}/atm) become comparable with the spacing between adjacent lines (typically 2 cm^{-1}) at pressures of the order of 10 atm. This results in an interference between lines, or line mixing, of rather complex nature. To better understand it qualitatively, we may assume that molecular collisions occur at random, and the duration of the collision is infinitesimally short. Between these brief collisions, a molecule is emitting or absorbing at a certain characteristic frequency. A molecule radiating at a given frequency before a collision may jump to a quantum state, which radiates at a different frequency as a result of the collision. This random jumping, or diffusion, between the lines, is called line mixing. The effect strongly depends on collisional coupling between rotational quantum levels and manifests itself in the transfer of spectral intensity from peripheral regions of the vibrational band to peak regions of the vibrational band. What is observed in the spectra is band narrowing, with higher absorption at the peaks and lower at the wings. In the limit of very high pressure, the rotational band structure collapses to a single rotational peak for each allowed spectral branch (P,Q,R, etc.)

Wing effect. The familiar Lorentzian lineshape of pressure-broadened spectral lines is based upon the impact approximation, which states that the dephasing collision occurs instantaneously fast. This assumption is valid when $\Delta\nu\times\tau<1$, where $\Delta\nu$ is the deviation from the line center, and τ is the collision duration (square root of optical cross section divided by the mean velocity). Quantitatively this means that, even for an isolated line, the Lorentzian lineshape is valid only within, perhaps, 3-10 wavenumbers from the line center. Beyond this range, the lineshape is expected to be sub-Lorentzian. This effect becomes very important at high pressures, when absorption at any wavelength within a band involves significant contribution from far wings of many spectral lines.

Collision-induced absorption (CIA). At high pressures, even molecules that are not normally infrared-active, become strong absorbers. To understand this effect, known since the 1940s, consider, for example, nitrogen. Although an isolated nitrogen molecule does not possess a dipole moment, it does possess a quadrupole moment. In a bimolecular collision, a dipole moment is induced in each of the molecules by the quadrupole field of the other, and dipole absorption becomes possible. Since the induced dipole moment is modulated by molecular vibration, rotation, and relative translational motion, vibrational-rotational (infrared), pure rotational (far-infrared), and translational (microwave) absorption bands become "allowed." At moderate pressure, the absorption coefficient increases as density squared. A typical absorption coefficient at the center of a fundamental band is of order $10^{-6} cm^{-1} Agt^{-2}$. At very high densities, however, three- and four-particle collisions become significant, partially compensating the two-particle effect and somewhat decreasing the absorption coefficient.

2.2. Sub-Lorentzian model.

As mentioned above, a consistent theoretical computation of absorption spectra with line mixing requires knowledge of not only spectral line positions, strengths, and broadening coefficients, but also of matrix elements of the relaxation operator responsible for rotational coupling between quantum states.[4-6] Formally, exact computations involve rather cumbersome, albeit standard, inversion of large matrices of state-to-state rate data. Since the rotational relaxation rates are often poorly known, this formally exact approach is still subject to considerable uncertainty. An even more serious problem is the fact that, at high pressures, the wing effect is equally as important as the line mixing. Mathematically, this results in a frequency dependent relaxation operator which presents a great difficulty for the theory.[4-6] Despite some recent theoretical developments, the theory is still far from being able to provide a simple and accurate predictive algorithm.[4]

At the same time, an empirical approach has been widely used for interpolation and extrapolation of infrared absorption spectra.[7-10] The approach is based on a

semi-empirical, sub-Lorentzian lineshape, with absorption coefficient, α, at frequency ν, calculated as:

$$\alpha = \sum_i \frac{S_i}{\pi} \frac{\gamma_i}{\gamma_i^2 + (\nu - \nu_{o,i})^2} \chi(|\nu - \nu_{o,i}|) \qquad (1)$$

where the sum is taken over all the transitions within the band; and S_i, $\nu_{o,i}$, and γ_i are the line intensity, position, and Lorentzian half-width, respectively. In Eq. (1), the Lorentzian lineshape function is multiplied by an empirical frequency-dependent correction factor, $\chi(|\nu - \nu_{o,i}|)$. The χ function, which accounts for line mixing and wing effects, is assumed to be constant for all lines within a given band, and is typically approximated by an exponential or polynomial expression with a few adjustable parameters. The parameters are evaluated by least-squares fitting of experimental data.

To represent the effect of spectral intensity transfer from wing-to-peak, the χ function should smoothly cut-off with increasing $|\nu - \nu_{o,i}|$, and be normalized so as not to alter the integrated absorption coefficient. The cut-off typically starts 2-8 cm^{-1} from the line center, dependent upon the Lorentzian linewidth, γ_i. Recently, a theoretical justification for the "corrected Lorentzian", or χ-function, approach, has been provided by Boissoles et. al., and by Roney.[4,5]

A normalized empirical χ function for CO_2 bands, suggested by Fukabori et.al., is given by:[10]

$$\chi = C, \qquad \text{for } |\nu - \nu_{o,i}| < \nu_m$$

$$\chi = C \frac{(\nu - \nu_{o,i})^2 + \gamma_i^2}{\nu_m^2 + \gamma_i^2} \left(\frac{\nu_m}{|\nu - \nu_{o,i}|} \right)^{\eta}, \qquad (2)$$

$$\text{for } |\nu - \nu_{o,i}| \geq \nu_m$$

where ν_m and η are empirical parameters, and C is a normalization constant given by:

$$C = \frac{\pi/2}{\left[\tan^{-1}\left(\nu_m/\gamma_i\right) \right] + \left[\frac{\nu_m}{\nu_m^2 + \gamma_i^2} \right] \left[\frac{\gamma}{\eta - 1} \right]}. \qquad (3)$$

Fukabori, et.al. found a reasonable agreement with their experimental data at 60 atm of pure CO_2 when $\eta = 3$ and $\nu_m = 8$ cm^{-1}.[10]

We have adopted this empirical lineshape and used it in a simple line-by-line, high-resolution transmission/absorption code. The new code will be calibrated by least-squares fits to experimental absorption measurements at high pressure (up to 1000 atm.) and temperature (up to 1000 K). These measurements are currently in progress. A preliminary result for the 2.7 micron CO_2 band in air at 123 atm and room temperature is shown in Fig. 1, along with HITRAN predictions. From Fig. 1, the band narrowing is clearly evident as increased absorption at line center and decreased absorption in the wings as compared to the Lorentzian HITRAN prediction. Dotted vertical lines on Fig. 1 correspond to some of the output frequencies of the HF and the nuclear-reactor-pumped Xe laser. Absorption for some of these lines will clearly be affected by band narrowing. The sub-Lorentzian code predictions, assuming $\eta = 3$ and $\nu_m = 2$ cm^{-1}, are indicated by the dotted line in Fig. 1. The overall agreement is quite good, although there is considerable difference at the two local minima.

In order to extrapolate to higher temperatures, the temperature dependence of η and ν_m will be investigated in future experiments. Theoretically, line mixing and wing effects are expected to be less important as temperature is increased, which implies an increase of ν_m with temperature.[4-6] Although a precise theoretical analysis has not been made from the physical interpretation of ν_m as dependent upon a combination of the mean rotational frequency and the reciprocal of a typical duration of an intermolecular collision, we can expect ν_m to be roughly proportional to the mean molecular velocity, and, therefore, to scale something like $T^{1/2}$. For the present, we assume, as a first-order approximation, that ν_m scales as $T^{1/2}$. Since the absorption is less inherently sensitive to the parameter η, we assume, for convenience, that it is independent of temperature. This will be investigated experimentally in the near future.

2.3. Collision-induced absorption model.

The theory of collision-induced absorption (CIA) is quite advanced. An extensive review is given in a recent monograph by Frommhold.[12] (See also Ref. [13] and [14], and references therein). The first step is to calculate the vibration-rotation line center positions and strengths nonempirically using quantum mechanics. Translational effects are accounted for by broadening each transition using a semi-empirical lineshape function, usually with four adjustable parameters. The parameters must be found by fitting to experiment. For low densities, the computations are more or less straightforward, although cumbersome. The biggest problem in the theory arises at high density, where there is significant contribution from many-body interactions. To our knowledge, there is currently no established simple algorithm for dealing with the many-body problem in conjunction with line-by-line spectral theory.

To compute collision-induced absorption in the fundamental band of nitrogen over a wide range of pressures and temperatures, we have developed a simple model, which is essentially the theory suggested several years ago by Joslin, with modifications based on results obtained earlier by Guillot and Birnbaum.[15,16] Although not as accurate as full line-by-line computation, the model is physically and

computationally simple, and, as we will see, can provide a reasonably good agreement with experiments.

Joslin's theory uses the well-known relation between the absorption coefficient, α, and the spectral intensity, $I(\nu)$,[15]

$$\alpha = \frac{16\pi^4}{3hc}\nu\left[1-exp\left(-\frac{h\nu}{kT}\right)\right]I(\nu), \qquad (4)$$

where c is the speed of light, and h and k are Planck's and Boltzmann constants, respectively. Joslin's theory uses classical mechanics together with the correspondence principle to calculate the spectral intensity. The classical expression is then multiplied by a statistical quantum factor:

$$S = \frac{2}{1+exp\left(-\frac{h\Delta\nu}{kT}\right)} \qquad (5)$$

where $\Delta\nu=\nu-\nu_{fund}$. The factor S, recommended by Poll, approximately accounts for quantum effects, enforces microscopic reversibility (detailed balance) requirements, and produces significantly asymmetric band shape.[17]

The spectral intensity is the Fourier transform of the total dipole moment (per unit volume) autocorrelation function. Since, in a first approximation, vibrational, rotational, and translational degrees-of-freedom are uncoupled, the autocorrelation function can be written as a product of a single-molecule, vibration-rotation correlation function, and a two-molecule translational term. Consequently, the spectral density is the convolution of vibration-rotation and translational spectra:

$$I(\nu) = \int_{-\infty}^{+\infty} d\nu'\, I_{vibrot}(\nu')I_{tr}(\nu-\nu'). \qquad (6)$$

The vibration-rotation spectrum can be calculated exactly, because it contains only single-molecule terms. The analytical expression can be found in Ref. [15]. To compute the two-molecule translational spectrum, Joslin suggested to apply information theory.[15] The information theory provides the "least biased" spectrum, based on available information on the spectral moments. Thus, the dynamical problem of calculating auto-correlation functions is reduced to the calculation of the first few moments of $I_{tr}(\nu)$, which is done by equilibrium statistical mechanics. What simplifies computations further is the fact that odd spectral moments vanish in the classical limit.

In our model, we made two modifications to the original Joslin theory. First, to compute the spectral moments, a knowledge of the two-particle radial distribution function (rdf) is required. When density is very high, on the order of liquid density, an explicit formula by Goldman can be used.[18] However, that formula is not valid for lower densities. We used the classical expression for the rdf in the low-pressure limit,

$$rdf \propto exp\left(-\frac{u(r)}{kT}\right), \qquad (7)$$

where $u(r)$ is the Lennard-Jones pair interaction potential. The low-pressure rdf was then matched to Goldman's formula at the lower limit of the latter's validity.

The second modification regards many-body encounters. Even for the zeroth and second spectral moments, an accounting should be made for three-body collisions, which reduces the accuracy, since the three-particle rdf is poorly known. For higher moments, encounters of four and more particles should be taken into account, which makes the calculations intractable. We, therefore, chose to ignore fourth and higher moments and to remove Joslin's three-particle terms in the zeroth, M_0, and second, M_2, moments.[19] Instead, we substituted a simple correction, suggested by Guillot and Birnbaum.[16] The two moments were multiplied by linearly decreasing functions of density, ρ. Specifically, M_0 was multiplied by $(1-\rho/\rho_o)$, and M_2 - by $(1-\rho/(2\rho_o))$, where the parameter ρ_o should correspond to a density somewhere between the close-packing and the solid density. For nitrogen, ρ_o is 800-900 Amagat.

With these modifications, we used Joslin's method with the molecular parameters (quadrupole moment, polarizability, moment of inertia, etc.) listed in Table 2 of Ref. [15]. To validate the model, we computed absorption in the collision-induced nitrogen fundamental band. The nitrogen fundamental CIA is of particular interest because this band overlaps some of the lines of DF laser. The results are shown in Fig. 2, along with experimental data of Reddy and Cho.[20] As seen from the figure, the agreement is very good, especially considering the simple nonempirical nature of the model.

3. MICROWAVE ABSORPTION IN HIGH-PRESSURE AIR

3.1. Basic mechanisms.

Assuming air above 50,000 feet consists of 79% nitrogen, 21% oxygen, and has small concentrations of CO_2 (330 ppm) and H_2O (5-10 ppm), there are three principle mechanisms for microwave absorption.

Oxygen absorption. The microwave spectrum of oxygen is due to a series of magnetic dipole transitions within the $^3\Sigma$ electronic ground state. Since the $^3\Sigma$ state has an unpaired electronic spin, the nuclear rotation (rotational quantum number N) couples to the electronic spin S=1 to produce a total angular momentum J which may take the values $J=N$, N-1, N+1. Transitions within the triplets form a broad band around 60 GHz (wavelength λ=5 mm). Motivated by the interest in

millimeter wave propagation through the atmosphere, this band has been extensively studied both theoretically and experimentally. The highest pressure at which measurements have been performed is, to our knowledge, 51 atm of pure oxygen at room temperature (Mingelgrin et. al., Ref. [21]). With increasing pressure, the band was observed to broaden, with the maximum shifting to lower frequencies. As a result, the absorption coefficient at 60 GHz grows linearly with pressure up to about 10 atm, and then remains nearly constant at 0.07-0.08 m^{-1}. Theoretical models, developed by Gordon,[22] Mingelgrin and Gordon,[23] Rozenkranz,[24] and Smith,[25] stress the importance of line interference (mixing), similar to that in the infrared spectra.

Collision-induced absorption. This effect is essentially the same as that discussed in section 2 for the infrared region. Since the transient dipole induced in a molecule by the quadrupole field of another molecule is modulated by the relative motion of the molecules, there is an absorption directly into translation. Both nitrogen and oxygen exhibit this effect, with nitrogen being more important due to its higher concentration in air. There is no specific resonant frequency, and microwave radiation of any frequency can be absorbed. As for the infrared CIA, the absorption strongly increases with density, and while the effect is negligible for normal atmospheric conditions, the absorption coefficient in liquid nitrogen reaches 0.1-0.4 m^{-1}.[26]

Free-electron absorption. Even if a relatively small number of free electrons are present in a gas, this may lead to considerable microwave absorption. The mechanism of an electron gaining energy from electromagnetic wave is essentially an inverse bremsstrahlung. This also may be thought of in simple classical terms as follows. The electric field of the wave imparts a directed velocity component on the electrons, which is superimposed on their random thermal motion. Collisional scattering of electrons by molecules randomizes this drift velocity, adding to the energy of thermal motion. At steady-state, the energy flow from the field to the electrons is balanced by electrons losing energy in elastic and inelastic collisions with molecules, resulting in gas heating. As we show later, fractional ionization as low as 10^{-8} can result in strong absorption. This weak ionization can be due to the natural thermal ionization present in air at temperatures of about 2500 K, when chemical contamination is not yet very high.

Before proceeding with quantitative models, it might be instructive to analyze some general features of microwave absorption as compared to the infrared. General formula for the absorption coefficient is given by Eq. (4) of linear response theory:

$$\alpha = \frac{16\pi^4}{3hc}\nu\left[1-exp\left(-\frac{h\nu}{kT}\right)\right]I(\nu)\,,$$

In this equation, the factor $(1-e^{-h\nu/(kT)})$, proportional to the difference in population of lower and upper quantum states participating in radiative transitions, reflects the net balance between absorption and stimulated emission. For infrared spectra, at low or moderate temperatures, $h\nu > kT$, and the factor $(1-e^{-h\nu/(kT)})$ is of the order of 1. In contrast, in the microwave region, where the frequency is 3 orders of magnitude lower than that of the infrared, $h\nu << kT$, and $(1-e^{-h\nu/(kT)}) \approx h\nu/(kT) << 1$. Physically, this means that because of the close spacing between states participating in microwave transitions, their populations are almost equal even at room temperature, and absorption is nearly balanced by stimulated emission. The general formula then reduces to:

$$\alpha \propto \nu\frac{h\nu}{kT}I(\nu) \qquad (8)$$

For molecular absorption, typical values of microwave spectral intensities, $I(\nu)$, should not be much different from that in the infrared bands. At high enough pressures, when bands are very broad, $I(\nu)$ becomes approximately constant. Also, at constant density, bands broaden with temperature approximately as $T^{1/2}$, and, therefore, spectral intensity near the band center decreases as $T^{-1/2}$. Thus, from our analysis we arrive at three general conclusions:

First, because microwave frequencies are 3 orders of magnitude lower than those of typical infrared bands, molecular microwave absorption is inherently much weaker than infrared.

Second, at high pressure, microwave absorption coefficients should be proportional to the square of the frequency.

Third, molecular microwave absorption coefficients should scale with temperature approximately as $T^{-3/2}$ at constant density, resulting in significant weakening of absorption with increasing temperature.

These conclusions refer only to molecular microwave absorption. Free-electron absorption behaves differently because of an inherently different behavior of $I(\nu)$. For example, if electrons are created by thermal ionization, then their concentration, and consequently, their absorption coefficient, exponentially increases with temperature. In addition, efficiency of electron energy gain from an electromagnetic field depends on the ratio of the field frequency to the electron-molecule collision frequency. When the period of electron oscillation induced by an alternating field is much smaller than the time between collisions, the collisions cannot efficiently convert the velocity of the fast oscillations into random thermal velocity. For this reason, efficiency of electron energy gain is the best in a constant electric field (zero-frequency limit). Therefore, the absorption coefficient should decrease with the field frequency, and free-electron

absorption is much stronger in the microwave frequency range than in the infrared.

3.2. Quantitative models of microwave absorption.

Oxygen absorption. As mentioned in section 3.1, rigorous theories exist to predict oxygen microwave absorption. However, these theories are very computationally intensive. In addition, they were developed for moderate pressures, and scaling with temperature was not analyzed. At high pressure, many-particle interactions may be important, which has never been considered. Therefore, in this paper, we use, as first approximation, simple extrapolation of experimental data. As mentioned previously, experimental data of Mingelgrin et. al. has demonstrated that at 60 GHz the room temperature absorption coefficient grows almost linearly up to about 10 atm, and then saturates, staying nearly constant.[21] Since 10 atm of pure oxygen corresponds approximately to 50 atm of air, (and working with density instead of pressure), we assume a linear increase of absorption coefficient with density up to 50 Amagat, and constant absorption coefficient for higher densities. The value for 50 Amagat of air at room temperature was taken from experiment.[21] For temperatures other than room temperature, scaling $(T/300)^{-1.4}$ was applied.

Collision-induced absorption. Calculations of collision-induced absorption coefficients were performed similarly to those for the infrared CIA, described in section 2.3. In fact, the microwave CIA computations are simpler than those for the infrared. Since the absorption is purely translational, only I_{tr} in Eq. [6] needs to be calculated. The first step in the model is to compute the zeroth, M_0, and the second, M_2, moments of the spectrum, which is done by a simple integration of the two-molecule rdf, $g(r)$:

$$M_0 = 3\left(\alpha_o^{(0)}\right)^2 Q_o^2 \rho^2 \left(1 - \rho/\rho_0\right) J_8 \qquad (9)$$

$$M_2 = 168\frac{kT}{m}\left(\alpha_o^{(0)}\right)^2 Q_o^2 \rho^2 \left(1 - \rho/2\rho_0\right) J_{10} \qquad (10)$$

where

$$M_2 = 168\frac{kT}{m}\left(\alpha_o^{(0)}\right)^2 Q_o^2 \rho^2 \left(1 - \rho/2\rho_0\right) J_{10} \qquad (11)$$

In these formulae, ρ is the density, ρ_0 is a parameter discussed in section 2.3, Q_0 and α_0 are molecular quadrupole moment and polarizability, respectively, k is Boltzmann's constant, and m is the mass of the nitrogen molecule. The spectral intensity and the absorption coefficient, α, are then calculated very simply:

$$I = I_{tr} = M_0\left(\frac{M_0}{2\pi M_2}\right)^{1/2} exp\left(-\frac{2\pi^2 M_0}{M_2}\nu^2\right) \qquad (12)$$

$$\alpha = \frac{16\pi^4\nu^2}{3ckT} M_0\left(\frac{M_0}{2\pi M_2}\right)^{1/2} exp\left(-\frac{2\pi^2 M_0}{M_2}\nu^2\right) \qquad (13)$$

Results of the calculation are shown in Fig. 3, where the collision-induced absorption coefficient is plotted versus density at various temperatures and two frequencies--60 and 110 GHz.

In fact, the absorption coefficient for the CIA need not be calculated at every value of temperature, density and frequency. We have found that, at fixed temperature, the absorption coefficient is approximated very well by the difference of two terms, the first being proportional to ρ^2, and second to ρ^3. Scaling of the room-temperature calculations as $T^{-1.4}$ reproduces results for higher temperatures with very good accuracy. As per Eq. [13], the frequency dependence is simply ν^2. Therefore, the absorption coefficient can be written as:

$$\alpha = \left(a\rho^2 - b\rho^3\right)\left(\tfrac{298}{T}\right)^{1.4}\nu^2, \qquad (14)$$

where coefficients a and b are found from calculations at room temperature and 60 GHz.

Free-electron absorption. General formula for the absorption of an electromagnetic wave in an ionized gas is given by Raizer as:[27]

$$\alpha = \frac{4\pi e^2}{mc} n_e \frac{\nu_m}{\omega^2 + \nu_m^2}\ , \qquad (15)$$

where n_e is the electron number density, $\omega = 2\pi\nu$ is the angular frequency of the electromagnetic wave, ν_m is the electron-molecule momentum-transfer collision frequency, e and m are electron charge and mass, and c is the speed of light. The collision frequency, proportional to the gas density, depends on electron energy. For air this dependence, according to Kroll and Watson, is:[28]

$$\nu_m(\varepsilon) = 7.0\cdot 10^{12}\frac{\varepsilon + 0.1}{\varepsilon + 4.94}\rho \quad sec^{-1}, \qquad (16)$$

where ε is the electron energy in eV, and ρ is the gas density in Amagat. For the average electron energy of 0.5 eV, and expressing ρ in terms of the number density, n, in cm^{-3}, we obtain: $\nu_m = 2.87\times 10^{-8} n$. For the microwave spectral range, at densities above 1 Amagat, the field frequency is much smaller than the collision frequency, $\omega << \nu_m$, and the absorption coefficient reduces to:

$$\alpha = 3.7 \cdot 10^8 \frac{n_e}{n} \quad m^{-1} \qquad (17)$$

The free-electron absorption coefficient, therefore, is proportional to the degree of ionization of the gas. Even very small ionization, such as 10^{-9}, would result in a significant absorption. This small ionization degree can be provided by the equilibrium thermal ionization existing in air at temperatures 2,500-3,000 K. At these temperatures, air contains 2-4% NO, which is primarily responsible for ionization because of the lower ionization potential of NO (9.26 eV) compared with that of nitrogen or oxygen. In the range 2,500-3,000 K, at moderate pressures, the time needed to establish chemical equilibrium in air is less than the typical flow time through the energy-addition region of RDHWT.[1] The degree of ionization, therefore, can be computed using standard equilibrium thermodynamic codes such as ASTRA. For example, at a pressure P=10 atm and temperature T=2,500 K, $n_e/n = 1.23 \times 10^{-10}$, while at T=3,000 K $n_e/n = 7.92 \times 10^{-9}$.

The degree of ionization can also be evaluated using Saha equation:[27]

$$\frac{n_e n_+}{n_a} = 2\frac{g_+}{g_a}\left(\frac{2\pi m k T}{h}\right)^{3/2} exp\left(-\frac{I}{kT}\right), \qquad (18)$$

where n_+ and n_a are number densities of positive ions and ionizable species, g_+ and g_a are their respective statistical weights, and I is the ionization energy. Assuming $n_e = n_+$, and that NO is the ionizable specie, an approximate formula for the free-electron absorption can be obtained. However, this formula does not take into account the existence of negative ions, and may somewhat overestimate the electron number density.

As discussed above, molecular absorption in the microwave spectral range is inherently weaker than in the infrared. Consequently, while infrared radiation can be absorbed in a single path of moderate length (order meters), complete single-path absorption of the microwave energy would require path lengths in excess of 100 m. For this reason, microwave energy addition will require some form of resonant cavity design where an intense electromagnetic standing wave could build-up, being, in a way, equivalent to a multiple-path system.

Another critical feature of the use of microwave energy is that the threshold power for dielectric breakdown of air is orders of magnitude lower than that for infrared radiation.[27] At normal atmospheric density, the threshold for microwave breakdown is of the order of 1 MW/cm^2. Fortunately, the breakdown threshold increases as the square of the desnity.[27] Consequently, the microwave power cannot be directed from downstream, as assumed in Ref. [1], since breakdown would occur in the low density region. The breakdown would create a plasma where microwave energy would be rapidly absorbed, stimulating undesirable plasma chemical reactions and preventing the microwave beam from passing to the high-pressure region.

One possible way to accommodate both the multiple cavity path requirement and restrictions imposed by the breakdown onset is to utilize a segmented cavity approach.[42] Slot reactances on the tunnel walls would act like mirrors, effectively creating a series of resonant cavities in the energy addition region. Since the cavities would be highly uncoupled from one another, and each cavity could be excited independently, this approach offers the capability of tailoring the energy addition profile. The field would be blocked, or significantly reduced, in order to prevent the onset of breakdown.

4. MECHANISMS OF MOLECULAR ENERGY TRANSFER AND THERMALIZATION

If an infrared laser is used as an energy source for the RDHWT, the energy is deposited initially into vibrational degrees of freedom of air molecules. To be efficiently used for flow acceleration, this energy must be quickly thermalized. However, vibration-translation (VT) relaxation is well known to be a relatively slow process, requiring many collisions. If the energy does not thermalize rapidly enough, it will not be converted into kinetic energy, and a significant nonequilibrium will exist at the test section. In addition, vibrational disequilibrium would trigger processes of quasi-resonant vibration-vibration (VV) energy exchange, which may strongly overpopulate highly excited vibrational states, and stimulate undesirable chemistry.[29,30]

Rates of VT relaxation and energy transfer among lower vibrational levels of nitrogen, oxygen, and CO_2 are known quite well.[30,31] Recently, models have been developed for relaxation involving highly excited states.[32] Both the models and data are valid for low and moderate densities, where relaxation is determined by binary collisions, and the mean free path is much larger than molecular diameters. In the RDHWT energy addition region, however, initial air densities are typically several hundred to several thousand Amagats, which is of the order of water or liquid nitrogen densities. In such a fluid, the distance between neighboring molecules is comparable to their diameter, and many-particle interactions are quite possible.

Over the last decades, many experimental and theoretical studies of vibrational relaxation in liquids have been performed.[33-41] One of the most important findings of these studies is the good accuracy of the isolated binary collision (IBC) model, which states that the probability of relaxation per collision in the liquid phase is close to that in the gas phase. The explanation for this is simple. In order for many-particle interactions and correlations to be important, the interval between consecutive collisions should be less than, or

comparable to, the collision duration. Since most collisions, at thermal energies, are inefficient to vibrationally relax, a "successful" relaxation collision requires kinetic energy an order of magnitude greater than kT. Since such energetic collisions are quite rare, the time interval between them turns out to be considerably longer than the collision duration. Hence, inter-collisional correlation is not significant.

To apply the IBC model, one should properly calculate the average collision frequency in terms of two-molecule rdf.[41] Because of the "excluded volume" occupied by molecules, the mean free path can be expected to be shorter, and the collision frequency--higher than that calculated by extrapolation of low density, gas-phase formulae. Therefore, while we can approximate relaxation rates as being proportional to density, we must keep in mind that this is a conservative estimate and that the actual high pressure relaxation time will be shorter than the extrapolated value.

Let us now consider the principal mechanisms of the relaxation process in high-density air absorbing HF laser radiation in the 2.7 micron spectral range. The process starts when a CO_2 molecule absorbs an HF laser photon resulting in simultaneous excitation of the bending (ν_2) and asymmetric (ν_3) stretch modes:

$$CO_2 + h\nu_{laser} \rightarrow CO_2(021) \qquad (19)$$

To supply the necessary enthalpy to the flow (typically 5-10 MJ/kg), and assuming a CO_2 concentration of 330 ppm, each CO_2 molecule must absorb on the order of 10^4 photons. This absorption must occur during the residence time in the energy addition region of the tunnel, which is typically 0.1-1 msec. The resulting average pumping rate is 10^7-10^8 photons/sec. If, as is likely, the energy addition profile is nonuniform, the maximum pumping rate may be even higher.

The CO_2 bending mode relaxes rapidly, with rate constant 1.6×10^{-13} cm^3/s at 1000 K, and even faster at 2000 K.[31] Consequently, the bending mode thermalizes in 2 ns at 10 Amagat, and 0.2 ns at 100 Amagat, which is an order of magnitude faster than the average pumping rate. However, if the energy addition rate is high in a region where density is of order 10 Amagat or lower, a saturation is possible, resulting in air becoming almost transparent to the laser beam.

Direct VT relaxation of the CO_2 asymmetric stretch mode is slow. Instead, energy can be transferred to the bending mode:

$$CO_2(001) + M \rightarrow CO_2(030) + M \qquad (20)$$

with subsequent thermalization. However the rate constant for this process is an order of magnitude smaller than that of near-resonant energy transfer to nitrogen:[31]

$$CO_2(001) + N_2(v=0) \rightarrow CO_2(000) + N_2(v=1) \qquad (21)$$

The rate constant for this process is 2×10^{-13} cm^3/s at 1000 K, and 10^{-12} cm^3/s at 2000 K.[31] Therefore, as with the relaxation of the bending mode, the CO_2-N_2 transfer is faster than the pumping rate at densities above 100 Amagat; however, at densities of the order of 10 Amagats or lower, the transfer rate may become equal to the pumping rate, implying the onset of saturation.

Once the vibrational energy is transferred to nitrogen, direct VT relaxation is slow, with rate constant of only 1.1×10^{-17} cm^3/s at 1000 K.[31] More efficient is the energy transfer to oxygen:

$$N_2(v=1) + O_2(v=0) \rightarrow N_2(v=0) + O_2(v=1) \qquad (22)$$

The rate constant for this process is 6×10^{-16} cm^3/s at 1000 K and 2×10^{-14} cm^3/s at 2000 K.[31] The time scale of this process is, therefore, 0.3 μsec at 1000 Amagat, 1000 K, increasing to 1 μsec at 10 Amagat, 2000 K. Assuming a pumping rate of 10^8 photons/sec per CO_2 molecule, and 330 ppm of CO_2 in air, a nitrogen molecule would receive quanta from CO_2 only once every 24 μsec. The nitrogen-oxygen transfer can, therefore, remove energy rapidly enough. However, once again, if the energy addition rate is high in a region where density is less than the order of 10 Amagats, or the temperature is below 2000 K, the transfer rate may become insufficient and vibrational nonequilibrium could occur.

The final stage of thermalization is oxygen VT relaxation:

$$O_2(v=1) + M \rightarrow O_2(v=0) + M \qquad (23)$$

with rate constant 1.6×10^{-15} cm^3/s at 1000 K and 10^{-13} cm^3/s at 2000 K.[31] The corresponding time scale is 23 nsec at 1000 Amagat, 1000 K, and 37 nsec at 10 Amagat, 2000 K. Consequently, this relaxation is much faster than nitrogen-oxygen transfer, and is not a limiting step in the overall relaxation process.

The following qualitative conclusions, relevant to IR lasers as the radiative energy source, can be drawn from our analysis. First, in the high-pressure region of the flow in the RDHWT, relaxation is fast enough so that no saturation or vibrational disequilibrium is expected. Second, in the moderate-density (about 10 Amagat) region, particularly at temperatures below 2000 K, both vibrational disequilibrium and saturation are possible. Third, the overall relaxation process has two possible "bottlenecks": CO_2-N_2 transfer is responsible for the saturation effect which would significantly reduce absorption, while in the absence of saturation nitrogen-oxygen energy transfer is the rate-limiting step.

5. RELAXATION MODEL

The observations and estimates made in the previous section allow us to use, as a first approximation, the following simple model. A single vibrational temperature, T_v, is ascribed to air molecules, and both the average vibrational energy per molecule, ε_v, and the relaxation equation are written in the harmonic oscillator approximation. The vibrational relaxation time is assumed to be determined by the nitrogen-oxygen transfer, so that:

$$\frac{d\varepsilon_v}{dt} = W - (\varepsilon_v - \varepsilon_o) k_{N-O} [O_2] \qquad (24)$$

$$\varepsilon = \frac{k\theta}{exp(\theta/T_v) - 1} \qquad (25)$$

where θ=3353 K is the N_2 characteristic vibrational temperature, $[O_2]$ is oxygen number density, ε_o is the equilibrium value of ε_v at $T_v = T$, W is the rate of energy absorption into the asymmetric stretch mode of CO_2, and k_{N-O} is the temperature-dependent rate constant of the nitrogen-oxygen transfer, equal to:

$$k_{N-O} = 7.03 \times 10^{-10} exp(-141 T^{-1/3}) cm^3/s$$

An estimate of the saturation effect can be made as follows. The fraction of nitrogen molecules in the ground vibrational level is $\left[1 - exp\left(-\theta/T_v\right)\right]$, and the fraction of CO_2 molecules in the first excited level of the ν_3 mode is $\left[1 - exp\left(-\theta_c/T_v\right)\right] \times exp\left(-\theta_c/T_v\right)$, where θ_c = 3407 K is the characteristic temperature of the ν_3 mode. Therefore, per CO_2 molecule, the rate of transfer to nitrogen is:

$$\nu_t = k_{C-N}(T) C_N n \cdot \left[1 - exp(-\theta/T)\right] \left[1 - exp\left(-\theta_c/T\right)\right] \cdot exp\left(-\theta_c/T\right) \quad , \qquad (26)$$

where:

$$k_{C-N} = 4.24 \cdot 10^{-24} T^{1/2} exp\left[10^{-3} T \left(8.84 \cdot 10^{-4} T - 2.07\right) + \frac{27}{T}\right] \ cm^3/s$$

is the rate constant of the CO_2-N_2 transfer, C_N is the molar fraction of nitrogen (approximately 0.79), and n is the total number density of air molecules.[30,31]

The number of photons absorbed per second by CO_2 molecules is:

$$\nu_a = \frac{\alpha P}{C_C n A h \nu_{laser} \left[1 - exp\left(-\frac{\theta_c}{T_v}\right)\right]} \quad , \qquad (27)$$

where P is the radiation power, α is the absorption coefficient, A is the cross section area, and C_C is CO_2 molar fraction. We require that ν_a be less than ν_t, which implies the following condition:

$$P < \frac{1}{\alpha} A C_C C_N n^2 h \nu_{laser} \left[1 - exp\left(-\theta_c/T_v\right)\right]^2 \cdot \left[1 - exp\left(-\theta/T_v\right)\right] exp\left(-\theta/T_v\right) k_{C-N} \ . \qquad (28)$$

If this flow condition is not satisfied, then the absorption process is subject to saturation.

Modeling results presented in Ref. [1] indicated that very significant energy addition occurred in a region where the density rapidly dropped from about 100 to 1 Amagat. This is a quite general phenomena reflective of the inherent loss in stagnation pressure associated with energy addition. This provides guidance in choosing optimum parameters for energy addition. Figure 4 shows the relaxation time plotted against temperature as a function of density. The shaded area represents the range of reciprocals of typical pumping rates. For the energy to thermalize successfully, the relaxation time at temperatures and densities corresponding to the high absorption rates should fall below the shaded area. If the temperature corresponding to the regions of significant pumping is too low, this condition may not be satisfied, and vibrational disequilibrium could occur.

CONCLUSIONS

Quantitative models for prediction of high pressure air absorption coefficients in both the infrared and microwave spectral regions, up to high pressures, have been developed. The models agree well with available experimental data, and can be further validated and corrected by comparison with future experiments. Analysis of molecular energy transfer processes in air under typical RDHWT conditions relevant to infrared energy addition has been performed. The analysis suggests that N_2-O_2 and CO_2-N_2 vibration-vibration energy transfer processes play key roles in thermalization of absorbed energy and, under certain conditions, may create "bottlenecks" in the relaxation process. Microwave energy addition in the RDHWT is influenced by relatively small absorption coefficients and limitations imposed by the onset of electric breakdown. This suggests the use of a segmented cavity approach to achieve the required energy addition.

ACKNOWLEDGMENTS

The authors wish to acknowledge a continued dialogue with Prof. Seymour Bogdonoff and Prof. Garry Brown, our colleagues on the RDHWT program. We would like to also express our gratitude to Dr. Howard Jory of Varian Corp., and to Dr. Preston Geren of Boeing, who have contributed their expertise in microwave technology and suggested a segmented cavity approach. This work was supported by the Air Force--Arnold Engineering Development Center and Wright-Patterson Air Force Base.

REFERENCES

1. R. Miles, G. Brown, W. Lempert, D. Natelson, R. Yetter, J. Guest, G. Williams, and S. Bogdonoff, "Radiatively Driven Hypersonic Wind Tunnel", accepted for publication in *AIAA Journal*, August 1995.

2. a) L.S. Rothman, *Appl. Opt.*, 20, 791 (1981); b) L.S. Rothman and L.D.G. Young, *J. Quant. Spectrosc. Radiat. Transfer*, 25, 505 (1981).

3. USF HITRAN PC, version 2.0, 1992. HITRAN Molecular Spectroscopy Database, Air Force Geophysics Laboratory/Phillips Laboratory.

4. P.L. Roney, *J. Chem. Phys.*, 101, 1037 (1994); *ibid.*, 101, 1050 (1994).

5. a) C. Boulet, J. Boissoles, and D. Robert, *J. Chem. Phys.*, 89, 625 (1988); b) J. Boissoles, V. Menoux, R. LeDoucen, C. Boulet, and D. Robert, *ibid.*, 91, 2163 (1989); c) J. Boissoles, C. Boulet, J.M. Hartmann, M.Y. Perrin, and D. Robert, *ibid.*, 93, 2217 (1990).

6. J.M. Hartmann, *J. Chem. Phys.*, 90, 2944 (1989).

7. B.M. Winters, S. Silverman, and W.S. Benedict, *J. Quant. Spectrosc. Radiat. Transfer*, 4, 527 (1964).

8. D.E. Burch, D.A. Gryvnak, R.R. Patty, and C.E. Bartky, *J. Opt. Soc. Am.*, 59, 267 (1969).

9. a) R. LeDoucen, C. Cousin, C. Boulet, and A. Henry, *Appl. Opt.*, 24, 897 (1985); b) C. Cousin, R. LeDoucen, C. Boulet, and A. Henry, *ibid.*, 24, 3899 (1985).

10. M. Fukabori, T. Nakazawa, and M. Tanaka, *J. Quant. Spectrosc. Radiat. Transfer*, 36, 265 (1986).

11. C. Meinrenken, et. al., (to be published).

12. L. Frommhold, "Collision-Induced Absorption in Gases", Cambridge Univ. Press, 1993.

13. Phenomena Induced by Intermolecular Interactions, Ed. by G. Birnbaum, NATO ASI series, Series B: Physics; vol. 127, Plenum Press, New York, 1985.

14. Collision- and Interaction-Induced Spectroscopy, Ed. by G.C. Tabisz and M.N. Neuman, NATO ASI series, Series C: Mathematical and Physical Sciences; vol. 452, Kluwer Academic Publishers, Dordrecht-Boston-London, 1995.

15. C.G. Joslin, *Can. J. Phys.*, 65, 1629 (1987).

16. B. Guillot and G. Birnbaum, *J. Chem. Phys.*, 79, 686 (1983).

17. J.D. Poll, in "Intermolecular Spectroscopy and Dynamical Properties of Dense Systems", Ed. by J. Van Kranendonk, North Holland Publishing Company, Amsterdam, 1980, p. 45.

18. S. Goldman, *J. Phys. Chem.*, 83, 3003 (1979).

19. C.G. Joslin, S. Singh, and C.G. Gray, *Can. J. Phys.*, 63, 76 (1985).

20. S.P. Reddy and C.W. Cho, *Can. J. Phys.*, 43, 2331 (1965).

21. U. Mingelgrin, R.G. Gordon, L. Frenkel, and T.E. Sullivan, *J. Chem. Phys.*, 57, 2923 (1972).

22. R.G. Gordon, *J. Chem. Phys.*, 46, 448 (1967).

23. U. Mingelgrin and R.G. Gordon, *J. Chem. Phys.*, 70, 3828 (1979).

24. P.W. Rozenkranz, *IEEE Trans. Antennas and Propagation*, AP-23, No. 4, p.498 (1975).

25. E.W. Smith, *J. Chem. Phys.*, 74, 6658 (1981).

26. I.R. Dagg, in: Phenomena Induced by Intermolecular Interactions, Ed. by G. Birnbaum, NATO ASI series, Series B: Physics; vol. 127, Plenum Press, New York, 1985, p. 95.

27. Yu.P. Raizer, "Gas Discharge Physics", Springer-Verlag, Berlin, 1991.

28. N.M. Kroll and K.M. Watson, *Phys. Rev.*, A5, 1883 (1972).

29. C.E. Treanor, J.W. Rich, and R.G. Rehm, *J. Chem. Phys.*, 48, 1798 (1968).

30. B.F. Gordiets, A.I. Osipov, and L.A. Shelepin, "Kinetic Processes in Gases and Molecular Lasers", Gordon and Breach, London, 1988.

31. P.F. Lewis and D.W. Trainor, "Survey of Vibrational Relaxation Data for O_2, N_2, NO, H_2, CO, HF, H Cl, CO_2, and H_2O", Final Report on ARPA Contract No. F04701-73-C-0284, AVCO Everett Research Laboratory, Everett, MA, 1974.

32. I.V. Adamovich, S.O. Macheret, J.W. Rich, and C.E. Treanor, *AIAA Journal*, 33, No.6, p.1064 (1995); *ibid.*, p.1070.

33. D.J. Russell and C.B. Harris, *Chem. Phys.*, 183, 325 (1994).

34. J. Chesnoy and G.M. Gale, *Ann. Phys. (Paris)*, 9, 893 (1984).

35. D.W. Lupo, H. Abdel-Halim, and G.E. Ewing, *Chem. Phys.*, 104, 455 (1986).

36. a) D.W. Chandler and G.E. Ewing, *J. Phys. Chem.*, 85, 1994 (1981); b) D.W. Chandler and G.E. Ewing, *J. Chem. Phys.*, 73, 4904 (1980).

37. C. Delalande and G.M. Gale, *J. Chem. Phys.*, 71, 4804 (1979).

38. S.R.J. Brueck and R.M. Osgood, Jr., *J. Chem. Phys.*, 68, 4941 (1978).

39. W.F. Callaway and G.E. Ewing, *Chem. Phys. Lett.*, 30, 485 (1975).

40. P.K. Davis and I. Oppenheim, *J. Chem. Phys.*, 57, 505 (1972).

41. P.K. Davis, *J. Chem. Phys.*, 57, 517 (1972).

42. H. Jory and P. Geren, (private communication).

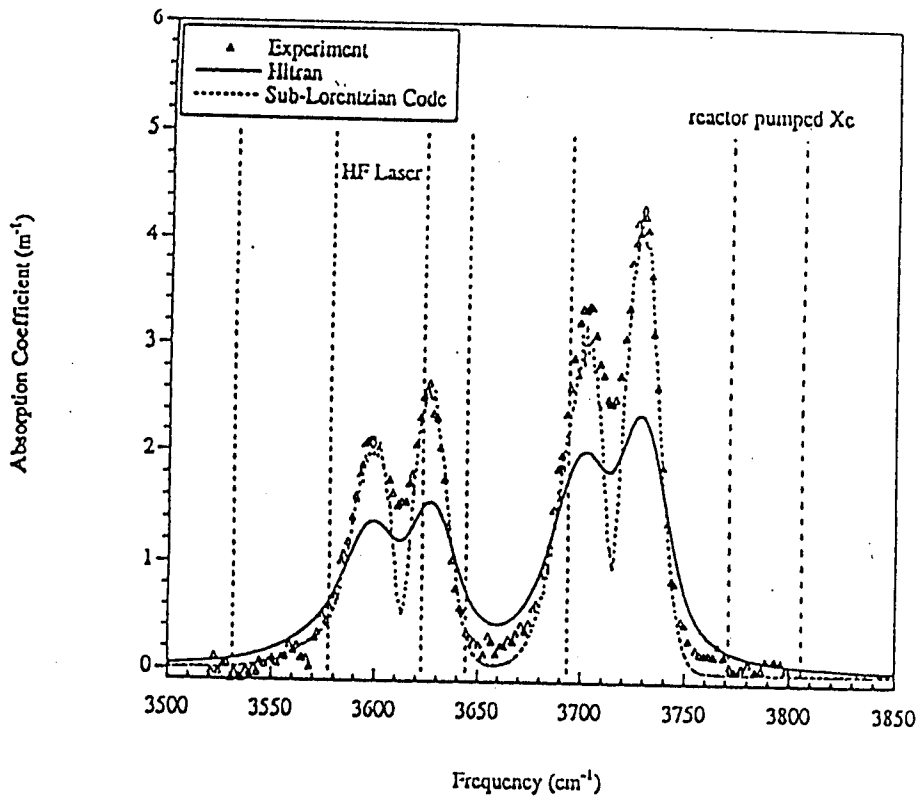

Fig. 1. Absorption spectrum of air at 123 atm, 300 K, in 2.7-micron CO_2 band. Vertical dashed lines indicate strong laser lines.

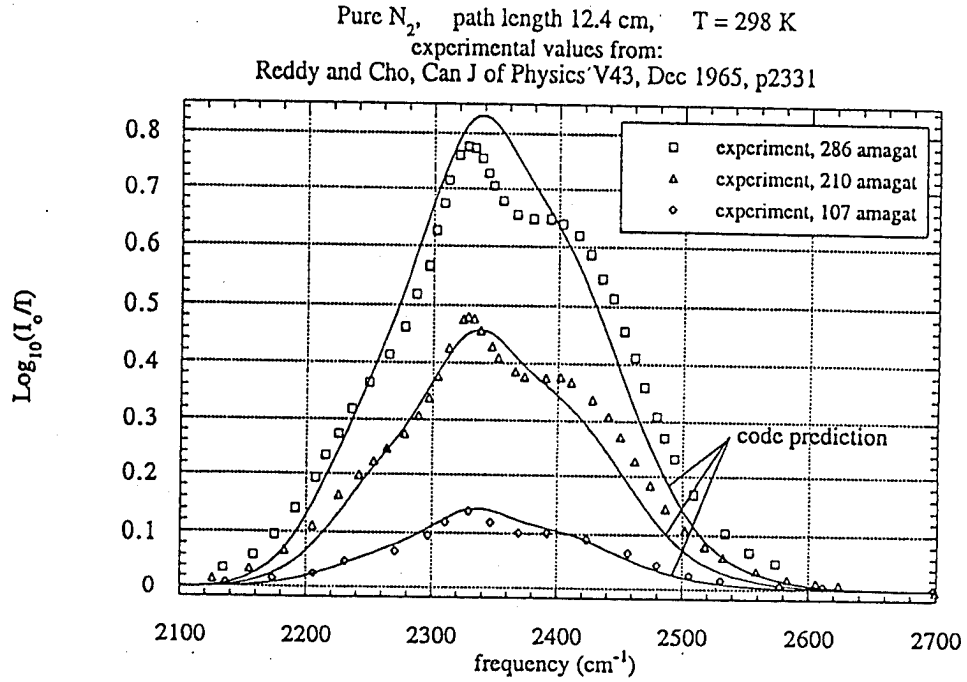

Fig. 2. Absorptivity in the nitrogen fundamental collision-induced absorption band. Solid lines--present theory. Diamonds, triangles, and squares--experimental data.

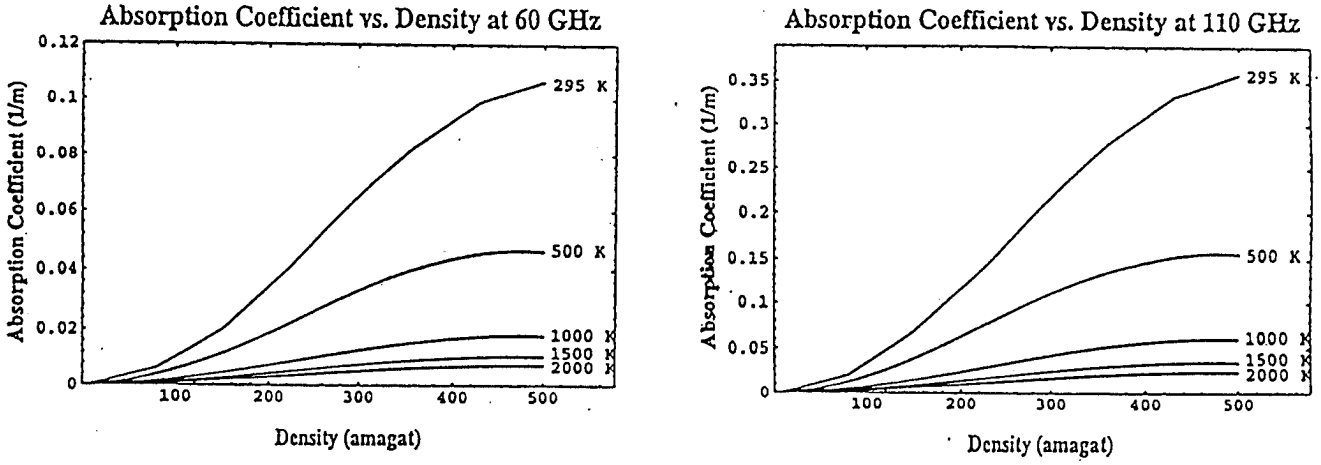

Fig. 3. Theoretical predictions for microwave collision-induced absorption in air.

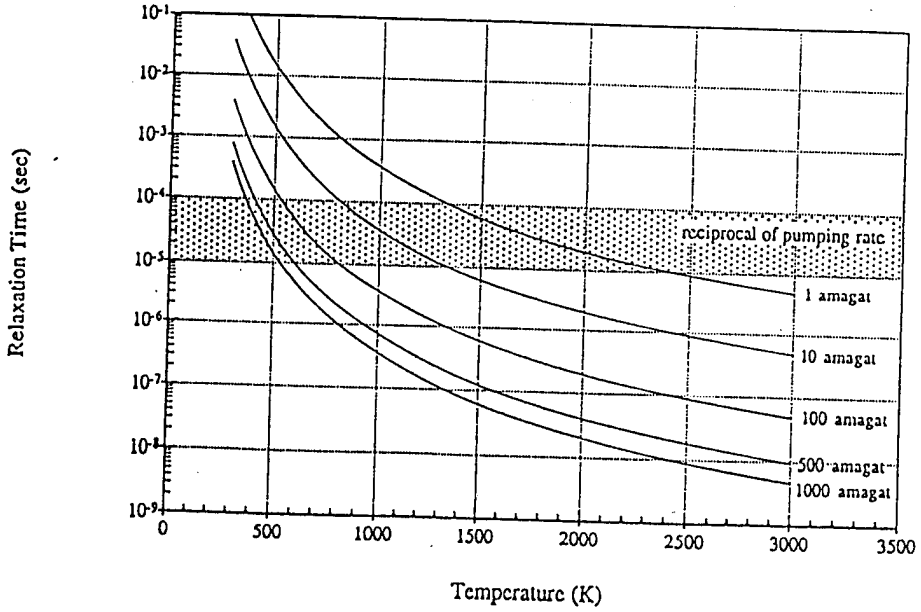

Fig. 4. Vibrational relaxation me of air vs. temperature at different densities. Shaded area corresponds to the range of reciprocals of photon absorption rate typical for the RDHWT.